

Latitudinal Controls on Topography: the Role of Precipitation and Fluvial Erosion

A Thesis

Presented in Partial Fulfillment of the Requirements for the

Degree of Master of Science

with a Major in Geological Sciences

in the

College of Graduate Studies

University of Idaho

by

Clayton S. Sorensen

Major Professor: Brian J. Yanites, Ph.D.

Committee Members: Eric L. Mittelstaedt, Ph.D; Elowyn M. Yager, Ph.D.

Department Administrator: Mickey E. Gunter, Ph.D.

April 2015

Authorization to Submit Thesis

This thesis of Clayton Sorensen, submitted for the degree of Master of Sciences with a Major in Geological Sciences and titled “Latitudinal Controls on Topography: the Role of Precipitation and Fluvial Erosion,” has been reviewed in final form. Permission, as indicated by the signatures and dates below, is now granted to submit final copies to the College of Graduate Studies for approval.

Major Professor: _____ Date: _____
Brian J. Yanites, Ph.D.

Committee
Members: _____ Date: _____
Eric L. Mittelstaedt, Ph.D.

_____ Date: _____
Elowyn M. Yager, Ph.D.

Department
Administrator: _____ Date: _____
Mickey E. Gunter, Ph.D.

Abstract

Observations from the North and South American Cordillera show that mean and maximum elevations decrease with latitude. A correlation between maximum elevation and ELA has been the impetus behind the glacial ‘buzzsaw’ hypothesis, which states that glaciers limit the elevation of mountain peaks. However, the expected latitudinal trend in topography in the absence of glacial processes is unknown. I use the CHILD model and NCEP/NCAR precipitation data along the Andes to predict trends in topography. Elevation trends vary along latitude by 2-30 fold, depending on the erosional and hydrological model parameterization. Trends generated using stochastic storm generation vary significantly from those generated using mean annual precipitation (MAP) suggesting that MAP may not capture the true geomorphic efficiency of the modern climate system. Geomorphic efficiency varies across the orogen as a result of orographic effects. The results provide further evidence in support of climate’s control on erosion processes and topography.

Acknowledgements

I would like to thank Brian J. Yanites for his guidance and support throughout my time at the University of Idaho and helping me obtain my Masters of Science in Geological Sciences. Thank you to my committee members Eric L. Mittelstaedt and Elowyn M. Yager. Funding for this project was provided by NSF award EAR-1251377 to Brian J. Yanites and a University of Idaho Department of Geological Sciences Teaching Assistantship supported Clayton S. Sorensen.

Dedication

I would like to dedicate this thesis to my parents, Neil L. and Pamela M. Sorensen. Without them, I would not be where I am today. Thank you Mom and Dad.

Table of Contents

Authorization to Submit Thesis.....	ii
Abstract.....	iii
Acknowledgements.....	iv
Dedication.....	v
Table of Contents.....	vi
List of Figures.....	viii
List of Tables.....	ix
Chapter 1: Introduction.....	1
Chapter 2: Methods.....	4
2.1 Model overview.....	4
2.1.1 Modeled storms.....	6
2.2 Model parameterization.....	7
2.2.1 Precipitation data.....	7
2.2.2 Erosional parameterization (Suites 1-8).....	9
2.2.3 Orographic runs (Suite 9).....	10
2.3 Model analysis.....	11
2.3.1 Grain size analysis.....	12
2.3.2 Threshold calculations and analysis of final modeled landscapes.....	13
Chapter 3: Results.....	16
3.1 Baseline runs (Suites 1-3).....	16

3.1.1 Lower critical shear stress for erosion (Suites 2 and 3).....	16
3.1.2 Mean elevations (Suites 1-3).....	17
3.2 Sensitivity tests.....	18
3.2.1 MAP runs (Suites 4 and 5).....	18
3.2.2 Decrease rock erodibility (Suites 6 and 7).....	19
3.2.3 Infiltration (Suite 8).....	21
3.3 Orographic runs (Suite 9).....	21
3.4 Model analysis.....	23
Chapter 4: Discussion	26
4.1 MAP vs. stochastic storms.....	26
4.2 The role of a critical shear stress for latitudinal trends in topography.....	29
4.3 Orographic influences on efficiency.....	31
4.3.1 Orographic differences.....	31
4.3.2 Infiltration differences.....	32
4.4 Comparison with modern topography.....	35
Chapter 5: Conclusion	37
References.....	38

List of Figures

Figure 1: Elevation profile of the Andes.....	41
Figure 2: Elevation map.....	42
Figure 3: CHILD mesh diagram.....	43
Figure 4: Graphical representation of precipitation statistics.....	44
Figure 5: Precipitation statistics.....	45
Figure 6: Cumulative distributions of storm statistics.....	46
Figure 7: Elevation trends for suites 1-3 and 8.....	50
Figure 8: Hypsometric curves (40, 45 and 50°S).....	51
Figure 9: Elevation trends for suites 4 and 5.....	52
Figure 10: Elevation trends for suites 6 and 7.....	53
Figure 11: Orographic storm statistics.....	54
Figure 12: Elevations for orographic runs (suite 9).....	55
Figure 13: Longitudinal profiles.....	58
Figure 14: Modeled slopes.....	59
Figure 15: Threshold slopes.....	60
Figure 16: Slope ratio.....	61
Figure 17: Precipitation threshold.....	62
Figure 18: Steepness index.....	63
Figure 19: Storm statistic inputs.....	64
Figure 20: Relative modeled elevations.....	65
Figure 21: Projected increase in uplift rate.....	64

List of Tables

Table 1: Suite classifications and naming scheme.....	47
Table 2: Input Parameters.....	48
Table 3: Inputs for grain size calculations.....	49
Table 4: Storm statistic inputs.....	56
Table 5: Orographic storm statistic inputs.....	57

Chapter 1: Introduction

The flow of water over a landscape is a fundamental control of erosion processes and therefore plays a central role in shaping topography. Ultimately, the flow of water is controlled by climate; larger amounts of precipitation result in larger amounts of water discharge within a landscape. This logic leads geomorphologists to postulate that climate controls erosion processes and topography, yet quantifying the degree to which climate controls topography has proven difficult [Riebe *et al.*, 2001; Ferrier *et al.*, 2013; Dadson *et al.*, 2003; Burbank *et al.*, 2003]. For example, some studies discover little to no correlation between climate gradients and erosion rates [Riebe *et al.*, 2001; Burbank *et al.*, 2003], while others successfully correlate spatially variable erosion rates with precipitation gradients [Dadson *et al.*, 2003; Ferrier *et al.*, 2013]. Such contradictions make climate's influence on geomorphology a central focus in many modern studies on landscape evolution.

The relationship resulting from quantifying climate's control on erosion process and topography has many implications on surface processes. The supply of sediment to the world's oceans and sedimentary basins, which are host to important petroleum resources, relies heavily on erosion rate [Leeder *et al.*, 1998]. Consequently, understanding how climate affects erosion process may provide better insight into climate's control over sediment supply. In addition, studies suggest that climate could be a strong factor in orogenic development as wetter climates may localize exhumation and crustal flow beneath the orogen while drier climates may drive a different style of orogenic evolution [Avouac and Burov, 1996; Beaumont *et al.*, 1992]. Therefore, by quantifying climate's control on topography, I can provide insight into the potential influence of climate driven erosion on tectonics. Finally, erosion and weathering are important components in greenhouse gas drawdown, potentially

driving long timescale climate changes [*Walker et al.*, 1981; *Zachos et al.*, 2008; *Raymo and Ruddiman*, 1992; *Maher and Chamberlain*, 2014; *Torres et al.*, 2014]. Therefore, understanding climate's control on erosion can help in understanding feedbacks within the climate-erosion system.

A common approach to deciphering the climatic influence on topography is to use latitudinal or other climatic trends along a single orogen as a natural experiment [*Montgomery et al.*, 2001]. Latitude is a fundamental control of climate and influences both the temperature and precipitation regime across a landscape. Maximum and mean elevations in the North and South American Cordillera decrease with latitude toward the poles (Figure 1 and 2). The elevation of snowlines and equilibrium line altitude (ELAs) also decrease with latitude, leading previous research to attribute the correlation between decreasing elevations and snowlines to an elevation limit imposed by glacial erosion, which has been termed the 'glacial buzzsaw' [*Montgomery et al.*, 2001; *Egholm et al.*, 2009; *Brozović et al.*, 1997; *Mitchell and Montgomery*, 2006]. According to the glacial 'buzzsaw' hypothesis, glaciers, which exist at lower elevations at higher latitudes, limit the growth of mountain peaks above the ELA [*Brozović et al.*, 1997]. However, the expected latitudinal trend in topography in the absence of glacial processes has not been addressed. In other words, how would elevation vary with latitude strictly under fluvial erosion and hillslope processes? Moreover, should we expect trends in topography with latitude prior to Quaternary glaciations?

I address the problem of the role of climate in controlling topography by parameterizing suites of numerical models using the Andes of South America as an example (Table 1). I create precipitation statistics using 31 years of global NCEP/NCAR precipitation magnitude data sampled every 6 hours. I extract storm statistics (i.e. mean storm intensity,

mean storm duration, and mean inter-storm duration) as well as mean annual precipitation rates at 10 locations spaced by five-degree latitude intervals (Figure 2). I use these statistics as climatic parameters in the CHILD landscape evolution model [Tucker *et al.*, 2001], while holding all other parameters equal. The models are run to dynamic equilibrium, and I extract mean and maximum elevations to predict the pattern of elevation with latitude if fluvial and hillslope processes were the only geomorphic process controlling topography. The results of my study demonstrate the geomorphic efficiency – defined as the amount of geomorphic work and measured by differences in maximum elevations – of the different climates along the latitudinal gradient of the Andes.

Chapter 2: Methods

2.1 Model overview

I use the Channel Hillslope Integrated Landscape Development (CHILD) model to predict topographic response to a variation of climate regimes along the Andes. CHILD uses a node-based, triangular finite-volume mesh to represent the surface of the landscape [Tucker *et al.*, 2001]. Each node is contained within a Voronoi polygon (or cell) and its surface area is equivalent to its Voronoi area. Each node is bisected by the edges of the Voronoi polygons (Figure 3) and each cell is assumed to have a channel. The model calculates runoff, discharge, shear stress, erosion (equations 1 – 2 and 6 – 7), and the change in elevation at each node.

The change in elevation at a node is based on the difference between erosion and rock-uplift for a given time step [Tucker *et al.*, 2001]. CHILD calculates fluvial erosion (E) along the steepest gradient between two nodes (Figure 3):

$$E = K(\tau_0^{P_b} - \tau_c^{P_b}), \quad \tau_0 > \tau_c$$

$$E = 0, \quad \tau_0 \leq \tau_c \quad (1),$$

where K is the rock erodibility coefficient [$\text{m yr}^{-1} \text{Pa}^{-1}$], τ_c is a user-defined critical shear stress (Pa) and P_b is an exponent relating shear stress to erosion [Whipple and Tucker, 1999] (see table 2 for parameter values). Erosion occurs at a node when the shear stress (τ_0) exceeds the critical shear stress. For all models, I assume detachment-limited erosion [Howard and Kerby, 1983]. Therefore, any sediment eroded from the bedrock is removed from the landscape. Because relief evolution is strongly dependent on the response of detachment-limited bedrock channels, this is a fair assumption [Whipple *et al.*, 1999].

Shear stress (τ_0) at a particular cell is calculated using discharge (Q) [m^3/yr], width (W) [m], and the slope between the two nodes (S):

$$\tau_0 = K_t \left(\frac{Q}{W} \right)^m S^n \quad (2),$$

where K_t is the shear stress coefficient [$\text{Pa s}^{1/3} \text{m}^{-2/3}$], where the units of K_t are dependent on m and n (parameters represented by mt and nt in table 2). We choose values for m, n and K_t to represent an excess shear stress model [Tucker *et al.*, 2001]. Channel width (W) is related to bankfull discharge (Q_b) [m^3/yr] [Leopold and Maddock, 1953]:

$$W = W_b \frac{Q^{w_s}}{Q_b} \quad (3),$$

where Q is the modeled discharge (see equation 6 below), and w_s is a parameter (see Table 2).

W_b and Q_b are the bankfull values for width and discharge, both scaling with drainage area:

$$W_b = k_w Q_b^{w_b} \quad (4),$$

$$Q_b = R_b A \quad (5),$$

where R_b is the bankfull runoff rate ($R_b = 13.6 \text{ m/yr}$), and R_b , k_w , w_b and w_s are constants and therefore Q_b and W_b do not vary at a given node during a model run (see table 2).

Runoff-driven erosion is only calculated during storm events. Precipitation is effectively translated to the landscape through runoff and is used to calculate the discharge (Q) at each node:

$$Q = RA \quad (6),$$

where A [m^2] is the contributing drainage area. R is the runoff [m^2/yr] and is the difference between precipitation intensity (I) [m/yr] and infiltration rate (i) [m/yr]:

$$\begin{aligned} R &= I - i, & I > i \\ R &= 0, & I \leq i \end{aligned} \quad (7).$$

In order for runoff to occur, the intensity (I) needs to exceed the infiltration rate.

2.1.1 Modeled storms

To model precipitation, CHILD uses a storm generator [Tucker *et al.*, 2001]. Each storm is discretely produced with a constant intensity (I) of finite duration (D), with consecutive storms separated by an inter-storm duration (F) (Figure 4). Intensity, duration, and inter-storm duration are assumed to be independent events and follow a Poisson distribution described by equations 8 – 10 below (Figure 4). CHILD uses the mean storm intensity, mean storm duration and mean inter-storm duration to calculate three separate probability density functions (PDF), one for intensity:

$$f(I) = \frac{1}{\bar{I}} \exp\left(-\frac{I}{\bar{I}}\right) \quad (8),$$

where \bar{I} is the mean storm intensity and is defined by the amount of water precipitated over the total time that it is raining. A second PDF is calculated for duration:

$$f(D) = \frac{1}{\bar{D}} \exp\left(-\frac{D}{\bar{D}}\right) \quad (9),$$

where \bar{D} is the mean storm duration and is defined as the average length of each storm.

CHILD calculates a third PDF for the inter-storm duration:

$$f(F) = \frac{1}{\bar{F}} \exp\left(-\frac{F}{\bar{F}}\right) \quad (10),$$

where \bar{F} is the mean inter-storm duration and is defined by the average time between storms.

CHILD randomly selects values from each PDF to create a storm and the precipitation generated during these storms is uniform across the landscape.

2.2 Model parameterization

2.2.1 Precipitation data

I use global reanalysis data, or assimilated and interpolated historical meteorological data, produced by the European Centre of Medium-Range Weather Forecasts to calculate storm statistics [ECMWF, 2009]. The data set is gridded into $0.75^\circ \times 0.75^\circ$ bins, and records

average precipitation every six hours for 31 years (1980 to 2010). The reanalysis data captures precipitation variability well [Decker *et al.*, 2011].

I calculate the mean storm duration, mean inter-storm duration, and mean storm intensity over the 31 years (Figure 5 a, b and c) and CHILD calculates intensity (I) and storm (D) and inter-storm (F) duration distributions based off of these means (equations 8 – 10). Although this stochastic model systematically over predicts the lower values for intensity, duration and inter-storm duration, it provides a reasonable approximation for the observed climate especially for the large and/or long lasting storms that are important for geomorphic processes (i.e. intensities that are greater than the infiltration rate; Figure 6) [Eagleson, 1978].

To calculate each storm statistic (i.e. mean intensity, mean storm duration and mean inter-storm duration), I define the start of a storm as beginning when a measurable precipitation magnitude occurs following an interval in which precipitation was zero (Figure 4). The storm is defined as complete at the next 6-hour period for which no rainfall occurs. This generates a 31-year time series of defined storm events. I also calculate the mean annual precipitation to test differences in climate regimes on topography (MAP; Figure 5d).

I draw 10 transects along the Andes at five degree intervals from 5°S to 50°S perpendicular to the coastline starting at the coast and across the full width of the orogen (Figure 2). I extract each precipitation statistic and average across each transect. I input these values into the climate parameters of the Channel Hillslope Integrated Landscape Development (CHILD) model.

2.2.2 Erosional parameterization (Suites 1-8)

To explore the influence of latitude and climate on geomorphic efficiency, I set up a control model run in which erosion parameters (rock erodibility and critical shear stress) are held constant across latitudes (Suite 1; Table 1). Values of rock erodibility were chosen such that reasonable dynamic equilibrium topography near the latitudes of the Atacama was achieved, as this is the location for the highest elevation in each trend for suites 1-3 and 6-8. Precipitation statistics at the 10 locations described above are used to drive the 10 different model runs representing the 10 latitudinal bands (Figure 2) to dynamic equilibrium. I refer to every set of 10 latitudinal distributed model runs as a suite (Table 1). To test the sensitivity of parameter choices on climate's influence on topography and elevation trends, I conduct eight suites varying critical shear stress and rock erodibility using the same extracted and averaged precipitation statistics along the Andes described above (Table 1). For all suites, I use a constant uplift rate of 0.5 mm/yr because it falls within observed ranges of uplift rates in the Andes [Gregory-Wodzicki, 2000; Benjamin et al., 1987]. All landscapes begin with a random topography with elevation <1 m. I run all models for 60 Myr to ensure each landscape reaches 'dynamic equilibrium', where erosion rate is equal to the uplift rate and elevations remain constant over long timescales. I set the node-spacing to 500 meters and the time step is defined as the duration of each storm [Tucker and Bras, 2000].

I amplify the storm and inter-storm durations by a factor of 10^3 - 10^4 for computational efficiency. This speeds up computation time, yet maintains the resulting landscape that will not differ significantly from a landscape produced without the factor increase [Tucker et al., 2001; Tucker and Bras, 2000]. The timescale of storm duration (10^0 - 10^2 years) to total model run (60 My) provides enough generated storms to sample a broad range of the precipitation

statistics. Each storm event simulates the cumulative effects of many events of the same intensity. Although the ‘culmination’ alters storm sequencing, it does not effect sampling of a broad distribution of storm sizes (intensities) and therefore plays a minor role in large scale landscape dynamics such as relative mean and maximum elevations in landscapes that have reached dynamic equilibrium [*Tucker and Bras, 2000*].

The eight suites test the effects of differing critical shear stress on geomorphic efficiency, the sensitivity to climate regimes, rock erodibility and infiltration on precipitation and geomorphic efficiency (Table 1). Suite 1 is what I refer to as the ‘control’ suite of the runs ($K = 1.25e-2$, $\tau_c = 50$). Suite 2 ($\tau_c = 5$) and 3 ($\tau_c = 0.5$) test the reduction of critical shear stress on geomorphic efficiency ($K = 1.25e-2$). Suite 4 ($\tau_c = 5$) and 5 ($\tau_c = 0.5$) test the sensitivity to MAP. Reasonable elevations using the MAP run required significantly reducing the rock erodibility ($K = 1e-5$), critical shear stress and infiltration ($i = 0$) since rainfall is constantly occurring. Suite 6 ($K = 2.8e-3$, $\tau_c = 5$) and 7 ($K = 2.5e-3$, $\tau_c = 0$) test the sensitivity to the rock erodibility coefficient (K) and require a reduction in critical shear stress to create reasonable elevations. Suite 8 ($K = 9e-5$, $\tau_c = 50$, $i = 0$) tests the sensitivity to the infiltration rate (i) and requires a reduction in the rock erodibility coefficient to create reasonable elevations (Tables 1 and 2).

2.2.3 Orographic runs (Suite 9)

Patterns of precipitation statistics observed in Figure 5d show clear variation across the orogen due to orographic effects [*Roe, 2005*]. To explore the implications of cross-orogen patterns of precipitation on geomorphic efficiency, I execute 18 additional runs to test across-width climate differences on erosion and elevation trends. I extract and average precipitation

statistics at three locations across the width of the Andes at 10°S, 20°S, 25°S, 30°S, 45°S and 50°S (Figure 2; Table 5). I choose these latitudes because they represent large across-orogen gradients in precipitation (Figure 5). Each run represents the climate recorded at a specific latitude and location across the width of the orogen – east, divide, and west (Figure 2). I keep rock erodibility (K) the same as in suite 8 to test the effect of across-orogen climate gradients on elevation trends. Because all other parameters are equal across runs, these across-width elevation trends represent the efficiency at which across-width climate gradients can translate to the landscape.

2.3 Model analysis

In order to provide insight into why different precipitation regimes produce various dynamic equilibrium topographies, I analyze final model topographies from each latitude of suites 1 and 8 in the context of the prescribed precipitation statistics. I extract river profiles from the headwaters to the outlet and calculate the rainfall intensity necessary to initiate erosion at each point along the river profile. Additionally, I determine the threshold slope necessary for erosion using the discharge that would occur during the mean precipitation event and compare this to the modeled steady state slope. Below, I now discuss these calculations in more detail. These analyses will provide insight into what magnitude of storm dominates the geomorphic processes. For example, is it the intense but rare, or low-intensity but frequent storms that do the most geomorphic work?

2.3.1 Grain size analysis

Suites 1 and 8 use a critical shear stress of 50 Pa. Shear stress that *exceeds* this value at a node represents the shear stress necessary to entrain a grain from the channel bed. Shields criterion is a unitless coefficient that is the ratio of shear stress to the density difference between a sediment grain and the water, the force of gravity and a grains diameter [*Shields*, 1936]. Theoretically, it is the ratio of the assumed driving forces to the resisting forces:

$$\theta = \frac{\tau}{(\rho_s - \rho_w)gD} \quad (11),$$

where τ is the shear stress, ρ_s is the density of the bedrock in kg/m^3 , ρ_w is the density of water, g is gravity and D is the grain diameter. Empirical data on the Shields criterion suggests a range of 0.03-0.06 [*Buffington and Montgomery*, 1997]. Rearranging equation 11 and substituting the critical shear stress (τ_c) for τ , I can calculate the threshold grain diameter entrained for the given τ_c . Assuming gravity equal to 9.8 m/s^2 and a density difference of 1650 kg/m^3 , I calculate that 50 Pa will entrain a grain diameter in the range of 5.15 to 10.31 cm (see table 3). This critical shear stress needs to be exceeded to generate erosion. Because shear stress in the river is a function of physical attributes of the landscape (equation 2) and the amount of precipitation delivered to the landscape, I can calculate what slopes and discharges are necessary to exceed this critical shear stress and initiate erosion. I base this analysis off modeled slopes extracted from landscapes in dynamic equilibrium and mean discharge and precipitation rates from the model outputs (see below).

2.3.2 Threshold calculations and analysis of final modeled landscapes

Equation 2 describes how CHILD calculates shear stress at each node. For model runs using a threshold for erosion, shear stress at the node needs to exceed this value for erosion to occur. Rearranging equation 2, I calculate threshold slopes using mean discharge and precipitation rates and threshold discharges using modeled slopes at each latitude for suites 1 and 8. This provides an estimate of the minimum slope and discharge necessary to do geomorphic work.

I extract node elevations, slopes and x,y- coordinates of large river channels within each model run from the baseline suite (Figure 13). Mean discharge (\bar{Q}) and width (W) scale with drainage area (A):

$$\bar{Q} = \bar{R}A \quad (12),$$

where \bar{R} is the mean runoff rate (m/yr) defined by

$$\bar{R} = \bar{I} - i, \quad \bar{I} > i \quad (13),$$

where \bar{I} is the mean storm intensity (m/yr) over the entire model run for storms *that exceed* the infiltration rate.

Rearranging equation 2 and using the above relationships between mean discharge, precipitation and width (equations 3 – 5 and 12 – 13), I determine the threshold slopes (\dot{S}) and discharges (\dot{Q}):

$$\dot{Q} = W_b \left(\frac{\tau_c}{K_t S^n} \right)^{\frac{1}{m}} \quad (14),$$

$$\dot{S} = \left(\frac{\tau_c}{K_t \left(\frac{\bar{Q}}{W_b} \right)^m} \right)^{\frac{1}{n}} \quad (15).$$

Threshold discharge (\dot{Q} ; equation 14) represents the discharge required to erode the bed using slopes extracted from landscapes in dynamic equilibrium. Where discharge exceeds \dot{Q} within a landscape, erosion will occur. Threshold slope (\dot{S} ; equation 15) represents the slope required to erode the bed using the mean discharge (\bar{Q} ; equation 12). Where the slope exceeds \dot{S} within a landscape, erosion will occur during the mean discharge event. I calculate threshold slope and discharge values along the longitudinal profiles of large rivers within each landscape from suite 1 and 8 using a critical shear stress of 50 Pa. See table 2 for parameters.

Using threshold discharge, I calculate threshold precipitation intensity needed to initiate erosion. To find this value, I rearrange equation 12 and equation 13:

$$\dot{I} = \frac{\dot{Q}}{A} + i \quad (16),$$

where \dot{I} is the threshold precipitation intensity and \dot{Q} is the threshold discharge (equation 14). Recall that i is the infiltration rate.

I calculate the steepness index to understand the relationship between slope and drainage area and how that might differ with latitude and its sensitivity to infiltration (suite 1

vs. suite 8). The steepness index (k_s) can be used as an important measure for uplift and erosion rates within channels in addition to providing slope information [e.g. *Wobus et al.*, 2006; *Ouimet et al.*, 2009] and describes the power law relationship between drainage area area (A) and slope (S) [*Wobus et al.*, 2006]:

$$S = k_s A^{-\theta} \quad (17),$$

where θ is the concavity of the longitudinal profile and is equivalent to the ratio of m:n. Both m and n are input model parameters (equation 2). Using modeled slopes (S) and rearranging equation 17, I calculate the steepness index (k_s) along profile and between latitudes.

Chapter 3: Results

3.1 Baseline runs (Suites 1-3)

I plot maximum and mean elevation from output landscapes versus latitude at ten locations along the length of the Andes (Figures 7, 9 and 10). First I consider the control case (suite 1) where I choose a rock erodibility coefficient (K) to generate maximum elevations at the driest latitude (25°S) to reach reasonable elevations (~ 4 km) with a τ_c of 50 Pa (Figure 7 a and b). Suite 1 shows lower elevations toward the equator (5°S to 15°S) where the climate generates the most vigorous geomorphic environment. Here, elevations range from 1.5 km (at 10°S) to 1.98 km (at 15°S). Elevations increase to the south with highest modeled elevations located at 20°S and 25°S . These landscapes modeled with precipitation from these latitudes are about twice as high as the landscapes to the north and range from 3.15 km (20°S) to 3.77 km (25°S). Elevations decrease to the south producing low elevations at 30°S , 35°S , and 40°S (Figure 7a). Elevations here are similar to the tropical landscapes and range from 1.45 km to 1.67 km. Modeled elevations south of 40° increase to ~ 3.1 km to 3.4 km at 45 and 50°S , respectively. For suite 1 ($K= 1.25\text{e-}2$ and $\tau_c = 50$), the difference in geomorphic efficiency generates an ~ 2.5 fold difference in total maximum elevation change (from 1.45 to 3.77 km at latitudes 30°S and 25°S , respectively).

3.1.1 Lower critical shear stress for erosion (Suites 2 and 3)

To test how differences in critical shear stresses affect geomorphic efficiency, I decrease critical shear stress to 5 Pa and execute an additional 10 runs (suite 2). The solid black line in Figure 7a represents runs using the same K and this reduced τ_c . Additionally, I decrease τ_c to 0.5 Pa and execute additional runs (suite 3; dashed black line in Figure 7a).

Although maximum elevations remain much lower for these variations, the trends follow a similar pattern: lower elevations are located near the equator (5°S to 15°S) and range from ~108 to 155 m (suite 2) and ~33 to 61 m (suite 3). Elevations increase to the south with the highest modeled elevations at 20°S and 25°S and are ~7 (suite 2) and 20 (suite 3) times as high as landscapes to the north and range from ~471 to 771 m (suite 2) and ~358 to 700 m (suite 3). Elevations decrease to the south producing low elevations at 30°S, 35°S, and 40°S (Figure 7), and are similar to the tropical landscapes and range from ~112 to 169 m (suite 2) and ~38 to 80 m (suite 3). Modeled elevations south of 40° increase to ~354 to 577 m (suite 2) and ~253 to 461 m at 45°S and 50°S, respectively. For suite 2 ($K=1.25e-2$ and $\tau_c = 5$) and suite 3 ($K=1.25e-2$ and $\tau_c = 0.5$), the difference in geomorphic efficiency generates an ~7 fold (suite 2) and ~21 fold (suite 3) difference in total maximum elevation change (from 108 to 771 m for suite 2 and from 33 to 700 m for suite 3).

3.1.2 Mean elevations (Suites 1-3)

Figure 7b represents mean elevations from suites 1-3. Although the mean elevation trends are similar to their maximum elevation trend counterparts, there is a distinct difference at a few latitudes between the max and mean trends for suite 1. Between 40°S and 45°S, maximum elevations increase significantly while the increase from 40°S to 45°S for mean elevations is steadier. The maximum elevation at 45°S, therefore, is much higher than the mean relative to 40°S and 50°S (Figure 7b). Hypsometric curves show that the majority of elevations at 45°S are lower than 40°S and 50°S (Figure 8). For a given elevation, the cumulative fraction of the total area is less for 45°S than for 40°S and 50°S (Figure 8).

3.2 Sensitivity tests

3.2.1 MAP runs (Suites 4 and 5)

I test the sensitivity of modeled elevation trends to the choice of precipitation regime by running suites of models with steady precipitation equal to the mean annual precipitation (MAP) (Figure 9), which is a common proxy for geomorphic efficiency in field-based studies focusing on climate's role on landscape evolution. I replace storm intensity with MAP, set storm duration to the length of the time step, and inter-storm duration to 0. I lower K to allow the location of the highest elevations within the suite 4 trend (now located at 35°S) to equal ~4 km using a critical shear stress of 5 Pa – model runs using a critical shear stress of 50 Pa could not produce reasonable topography in dynamic equilibrium, as they required extreme slopes for the latitudes with particularly dry climates. I use this K to execute suite 5 (0.5 Pa). Additionally, I set infiltration rate equal to 0 m/yr as MAP values tend to be lower than typical infiltration rates. By turning off the stochastic storm generation function and with the specified climatic parameters above, I essentially set CHILD to produce a constant storm through time with the precipitation rate equal to the MAP.

Maximum elevations are lowest toward the equator (5°S to 15°S) and range from 1.49 km (at 5 °S) to 1.65 km (at 15°S) for suite 4 and 1.22 km (at 10°S) to 1.37 km (at 15°S) for suite 5 (Figure 9a). Elevations increase from 15°S to 20°S to 3.49 km (suite 4) and 2.82 km (suite 5), ~ 2 times higher than elevations to the north. Elevations decrease at 25°S and 30°S to 2.79 (suite 4) and 2.31 km (suite 5) before increasing again from 30 to 35°S to the maximum elevations for both suites (4.27 km for suite 4 and 3.4 km for suite 5). From 40°S to 50°S elevations decrease and remain at a rather constant elevation ranging from 2.22 km (at 45°S) to 2.57 km (at 50°S) for suite 4 and 1.82 km (at 45°S) to 2.21 km (at 50°S) for suite 5

(Figure 9). For the MAP model runs ($K = 1e-5$ and $\tau_c = 5$ and 0.5), the difference in geomorphic efficiency generates an ~ 2.8 (suite 5) to 2.9 (suite 4) fold difference in total maximum elevation change (from 1.49 to 4.27 km for suite 4 and 1.22 to 3.4 km for suite 5). Mean elevation patterns follow maximum elevation patterns for the MAP runs (Figure 9b). Elevations range from 608 m to 1.39 km (suite 5) and 684 m to 1.68 km (suite 4) and the difference in geomorphic efficiency produces an ~ 2.5 (suite 4) and ~ 2.3 (suite 5) fold difference in mean elevation change (Figure 9b).

3.2.2 Decrease rock erodibility (Suites 6 and 7)

I explore the effect of erodibility on maximum elevation difference in suites 6 and 7. Decreasing rock erodibility requires a lower threshold for maximum elevations at 25°S to obtain an elevation of ~ 4 km (τ_c of 5). By lowering rock erodibility and critical shear stress, absolute elevations decrease significantly at tropical (5 - 15°S) and mid latitudes (30 - 40°S), and only slightly decrease at subtropic and high latitudes (20 , 25 , 45 and 50°S), resulting in an *increase* in the maximum elevation difference (Figure 10). For the suite 6 ($K = 2.8e-3$ and $\tau_c = 5$) model runs, the difference in geomorphic efficiency generates an ~ 17 fold difference in total maximum elevation change (from 234 m to 4.09 km). Therefore by lowering K , the range in maximum elevations increases by a factor of 6.5 (from suite 1 to suite 6). Although the elevations follow the same general pattern as suite 1 of the baseline runs, there is a distinct difference: the relative change in elevation between the highest and lowest points is much more pronounced for suite 6 (Figure 10a). The difference along orogen is also greater compared with suite 2 which also used a critical shear stress of 5 and only saw a 7 -fold difference in elevation.

Mean elevations for suite 6 follow the same pattern as the maximum elevations (Figure 10b). The difference in geomorphic efficiency generates an ~18 fold difference in mean elevation (from 87 m to 1.53 km).

The dashed gray line represents the trend produced by suite 7 (Figure 10 a and b). Again, I lower K from suite 1 to allow maximum elevations at 25°S to reach about 4 km using a τ_c of 0. Maximum elevations equal 4.53 km (25°S), minimum elevations equal 148.91 m (10°S), and the total maximum elevation difference is 4.39 km (Figure 10a). The trend is very similar to the suite 6 trend in its shape and elevations. For the suite 7 ($K = 2.5e-3$ and $\tau_c = 0$) model runs, the difference in geomorphic efficiency generates a ~30 fold (suite 7) difference in total maximum elevation change (from 149 m to 4.53 km). The difference along orogen is also greater compared with Suite 3, which used a similar critical shear stress ($\tau_c = 0.5$ Pa) and only saw a 21-fold difference in elevation (Figures 7 and 10).

Mean elevations for suite 7 are shown in the trend presented in Figure 10b (solid gray line). The difference in geomorphic efficiency generates a ~31 fold difference in total maximum elevation change (from 56 m to 1.74 km).

The trends produced by Suite 6 and Suite 7 runs are almost indistinguishably similar. When compared to suite 1 and suite 2 and 3, these two trends have a much larger difference in elevation between the highest and lowest points. Maximum elevations for suite 1, suite 6 and suite 7 are all located at 25°S and within 768.1 m (Figure 7 and 10). These differences in elevation at 25°S are minimal. Elevations in the tropical and mid latitudes (i.e. 10°S, 15°S, 30°S, etc.) for suite 6 and 7 are much lower when compared to the suite 1 suggesting that precipitation has a significant impact with the decrease in critical shear stress and rock erodibility coefficient (Figure 7 and 10). There is a ~17 and 30 fold difference in elevation

between the highest and lowest points for suites 6 and 7. The total maximum elevation difference increases from 2.6 fold to a ~17 fold, a factor of ~6.5, from suite 1 to suite 6 by decreasing K by $9.7e-3$ [$m\ yr^{-1}\ Pa^{-1}$] and decreasing critical shear stress by an order of magnitude (50 Pa to 5 Pa; Figure 7, 10 and table 1). The total maximum elevation difference increases from 2.6 to ~30 fold, a factor of ~11.5, from suite 1 to suite 7 with a decrease in K by $1e-2$ [$m\ yr^{-1}\ Pa^{-1}$] and a decrease in critical shear stress to 0 Pa.

3.2.3 Infiltration (Suite 8)

Next, I test the sensitivity of geomorphic efficiency to a decreased infiltration rate by setting it to 0 [$m\ yr^{-1}$] (suite 8). Again, I choose a K such that the driest latitude will contain elevations about equal to 4 km. Figure 7 shows the results of suite 8 with a K of $9e-5$ [$m\ yr^{-1}\ Pa^{-1}$] and a critical shear stress of 50 Pa. Mean and maximum elevations are similar to suite 1: low elevations from 5 to 15°S and increased elevations at 20 and 25°S (Figure 7 a and b). The major difference lies at elevations from 30 to 50°S: the trend here is rather flat, ranging from 2.01 km to 2.4 km (Figure 7). Compared to suite 1, elevations are higher at 30, 35 and 40°S and lower at 45 and 50°S. Additionally, elevations increase more gently from 40 to 50°S (Figure 7). However, differences in maximum elevation magnitudes are fairly similar as no infiltration results in a 2.2 fold difference between 5 and 25°S (Figure 7).

3.3 Orographic runs (Suite 9)

Variability in precipitation occurs across-orogen in addition to across-latitude (Figure 5). Precipitation intensity is high with a low variability at 10°S, while the storm to inter-storm duration ratio (D:F) is also high across the orogen (Figure 11; Table 5). D:F and storm

intensity increases from West-East across the orogen at 20, 25 and 30°S and East-West across the orogen at 45 and 50°S (Figure 11; Table 5). Precipitation intensity is moderately variable at 20 and 30°S and highly variable at 25, 45 and 50°S (Figure 11).

Results show significant across-width differences in geomorphic efficiency at 25°S, small differences at 10°S and moderate differences at 20, 30, 45, and 50°S (Figure 12). Across-orogen trends at 20, 25 and 30°S pin the most significant geomorphic efficiency at the East, decreasing to the West. At 45 and 50°S geomorphic efficiency is most significant starting at the East and decreasing to the West. At 10°S geomorphic efficiency is about equal at the West and East and is more significant at the divide (Figure 12).

Toward the equator, maximum elevations are low with little variation resulting in constant geomorphic efficiency across the orogen (Figure 12). Elevations range from 1.56 km (divide) to 1.79 km (west) at 10°S, an ~1.15-fold difference (Figure 12). Variation in elevation increases at 20 and 25°S where maximum elevations are located in the West and decrease to the East, resulting in an increasing trend in geomorphic efficiency from West to East (Figure 12). Elevations range from 1.96 to 4.97 km (at 20°S) and 1.51 km to 22.31 km (at 25°S) resulting in a ~2.5-fold (20°S) and 14.8-fold (25°S) difference in maximum elevation across the orogen (Figure 11). Elevation decreases from West to East and ranges remain moderate at 30°S, resulting in increasing geomorphic efficiency West to East. Orographic precipitation predicts the range in elevation from 1.51 to 3.45 km and a 2.29-fold difference across the orogen (Figure 12). The trends in elevation change at 45 and 50°S – maximum elevations are now located in the East and decrease to the West across the orogen, resulting in decreasing geomorphic efficiency West to East (Figure 12). Here, orographic precipitation predicts elevation ranges from 1.45 to 2.89 km (45°S) and 1.32 to 3.92 km

(50°S), resulting in a ~2-fold (45°S) and ~3-fold (50°S) difference in maximum elevation (Figure 12).

3.4 Model analysis

I analyze dynamic equilibrium topography of all 10 runs from both suite 1 and 8 to provide insight into why different precipitation regimes produce the various topographic trends. Longitudinal profiles of rivers within each landscape are plotted in Figure 13 a and b. Tropical latitudes (5, 10 and 15°S) and mid latitudes (30 and 35°S) contain smoother profiles (Figure 13a), while subtropical (20 and 25°S) and upper-mid (45 and 50°S) latitudes contain steeper slopes toward the headwaters (Figure 13a). Channels that do not use an infiltration rate are overall smoother with lower slopes toward the headwaters (Figure 13b). The dashed lines in Figure 13a represent the maximum elevation from the model runs at 40°S, 45°S and 50°S in suite 1 (Figure 13a).

Slope and discharge both influence river shear stress – as discharge increases along the channel flow path, slopes must adjust to produce uniform erosion rates (Figure 14). Therefore, the threshold values must follow similar trends (Figure 15 a and b). Tropical and mid latitudes (5, 10, 15, 30, 35, and 40°S) contain slopes that are on average lower (Figure 14 a and b), resulting in higher threshold discharge values. Subtropical to upper-mid latitudes (20, 25, 45 and 50°S) result in the opposite relationship: threshold slopes are larger and threshold discharge is lower (Figure 15).

Similar to threshold slopes, the ratio between modeled slopes and slope thresholds ($S_m:S_t$) also decreases with distance along the river channel and in the tropical and mid latitudes (5, 10, 15, 30, 35 and 40°S) and increases in the subtropic to upper-mid latitudes (20,

25, 45 and 50°S; Figure 16). For suite 1 runs, at about 15-20 km along the channel, the modeled slopes become less than threshold slopes at tropical and mid latitudes, and vary heavily above and below the 1:1 line at subtropical and upper-mid latitudes (Figure 16a). Values have a lower range and stay below the 1:1 line for suite 8 runs (Figure 16b), except for at 25°S, where the majority of values vary more and remain above the 1:1 line. Modeled slopes and the slope ratio vary to a higher degree for suite 1 runs (Figures 14 and 16).

Figure 17 (a and b) shows the threshold amount of precipitation rates required to generate erosion. Similar to threshold discharges, threshold precipitation is larger at tropical and mid latitudes (i.e. 5, 10, 15, 30, 35 and 40°S), indicating that larger magnitude storms are required to initiate erosion, as the slopes are lower (equations 14 and 16; Figure 17). Precipitation threshold increases with distance along the longitudinal profile and varies with local slope (Figure 17). Threshold values are larger and more varied for suite 1 (Figure 17a). The main channel within 25°S sits well below and has a higher variation than the rest of the other latitudes for suite 8 (Figure 16b).

For spatially uniform precipitation, the steepness index along a channel should be constant [*Han et al.*, 2015]. Values for steepness index remain constant toward the headwaters and become increasingly variable with distance along the channel for suite 1, likely due to artifacts from the increased storm and inter-storm durations I applied for computational tractability (Figure 18a). Model runs within suite 8 experience a larger distribution of storms because these model runs did not have an infiltration rate. Because of this, landscapes are able to adjust to the larger number of storms by smoothing river profiles (Figure 13b) and steepness indices (Figure 18). The suite 8 landscapes all remain rather constant with the exception of 25°S (Figure 18b). The tropical to mid latitudes (5, 10, 15, 30, 35, and 40°S)

generally contain smaller steepness values compared to the subtropics to upper-mid latitudes (20 to 25, and 45 to 50°S).

Chapter 4: Discussion

Climatic patterns in precipitation characteristics predict significant differences in elevation as a function of latitude (Figure 7, 9 and 10). The differences in elevation for a given suite show that climate has a first order control on elevation and topography. For a given model suite, the only change in input parameters between model runs (representing the latitudes) is the precipitation statistics. Therefore, differences in elevation within a suite of model runs are the direct result of differences in climate, specifically storm intensity, storm duration, and inter-storm duration. The trends and their differences in elevation highlight the ability of precipitation gradients to produce significant elevation trends resulting from gradients in geomorphic effectiveness. If a storm's precipitation intensity is able to overcome the imposed critical shear stress by delivering enough discharge to the landscape, erosion will occur. Where erosion can occur more frequently and over large periods of time (duration), elevations within topography will decrease. Therefore decreases in topography in the modeled trends occur in the tropical (5, 10 and 15°S) and mid latitudes (30 and 35°S) with large storm intensities (5, 10, 15, 30 and 35°S) and large duration (5, 10 and 15°S) where inter-storm duration is smaller (Figure 19).

4.1 MAP vs. stochastic storms

Mean annual precipitation (MAP) and stochastic storm generation produce different elevation trends between latitudes 25 and 50°S but similar trends from 5 to 20°S (Figure 7, 9 and 10). The divergence in trends in some regions suggests that MAP may not capture the true geomorphic efficiency of the climate in these latitudes (Figures 7 and 9). Additionally, peak elevations lie at different latitudes – at 25°S for the stochastically generated trends (Figures 7

and 10) and at 35°S for the MAP-generated trends (Figure 9). These differences in elevation trends imply that there is a fundamental difference between runs that use MAP (suites 4 and 5; Figure 9) and those generating storms (suites 1-3, 6 and 7; Figures 7 and 10).

The divergence in trends is likely due to changes in intensity and the ratio of duration to inter-storm duration (D:F) with latitude (Figure 19). From 5 to 15°S, mean storm intensities and D:F are large (Table 4; Figure 19), suggesting frequent, intense storms. Because MAP is also large at these latitudes (Table 4; Figure 19), it models the high intensity and low variability from the stochastic runs, matching the stochastically generated suites (Figure 7 and 10). The trends differ significantly starting at 30 and 35°S (i.e. 35°S goes from one of the lowest locations in suite 1 to the highest for suites 4 and 5). Here, mean storm intensities remain high and D:F ratios decrease (Figure 19). The change in intensity and duration suggests that storms become more intense but less frequent (i.e. more time between each storm). Therefore as storms occur, however infrequently, they deliver enough precipitation to the landscape to overcome the critical shear stress and generate erosion. However, because MAP is reduced because of the longer inter-storm duration time, it does not capture the geomorphic effectiveness of high intensity events that occur on a regular basis. Although it rains infrequently the storms that do occur do so with significant intensity to exceed threshold such that elevations are lower in the stochastic runs compared to MAP runs (Figure 10). Precipitation threshold values confirm the necessity of large discharge events to initiate erosion (Figure 17), while agreeing with previous research as erosion can be dominated by large discharge events [Tucker, 2004]. Therefore, since the elevation trends differ significantly, it suggests that the trends in MAP (Figure 19a) are not enough to correctly capture the true geomorphic efficiency conveyed to the landscape by the stochastic storms.

The difference in trends and its cause suggests that storm intensities play a large role in erosion and that large intensity values dominate geomorphic efficiency when D:F ratios are low (i.e. 30 and 35°S; Figure 19 and Table 4). MAP rates are low and therefore do not deliver large precipitation rates to the landscapes at 30°S and 35°S (Figure 19). These MAP values do not match the high intensity precipitation rates delivered to these landscapes by the stochastic runs at 30°S and 35°S (Figure 19). Therefore, the differences in elevation highlight the importance of large precipitation intensities that are not conveyed to the landscapes by MAP.

It has been argued that the stochastic nature of storms is necessary to properly model landscape evolution [*Tucker, 2004; Tucker and Bras, 2000*], yet comparison of topography with storm statistics in natural landscapes is rare [e.g. *Jeffery et al., 2014; Bookhagen et al., 2005*]. Therefore, it may be necessary to look at precipitation statistics and climate variability when comparing topography along a climate gradient in order to infer the influence of climate on topography. For example, studies that attempt to correlate climate with spatially variable erosion rates use MAP [i.e. *Riebe et al., 2001; Burbank et al., 2003*]. The location of these studies fall within the mid-latitude range where precipitation intensities remain large and MAP decreases (Figure 19), while studies successfully correlating climate with erosion [i.e. *Ferrier et al., 2013; Dadson et al., 2003*] are located in the tropical latitudes where MAP models the high intensity and frequent storms well (Figure 7 and 9). The results suggest that using MAP might not fully represent the geomorphic effectiveness of climate and I argue that one must be careful when using MAP in modeling landscape evolution as the output landscapes will differ significantly from landscapes using stochastically generated storms (Figures 7 and 9).

Ultimately, I produce very different latitudinal trends using MAP and stochastically generated storms. These results imply that more research needs to be focused on the implementation of climate through both of these methods. Because trends match in certain locations (i.e. the tropics) but do not in others (i.e. the mid and upper-mid latitudes), this suggests that in certain locations MAP successfully delivers stochastic signals to the topography while in others it does not. Therefore, I cannot discount MAP as an appropriate proxy for climate driven erosion in some locations. More importantly, I produce numerical evidence suggesting that using MAP may not capture important climatic signals that appear when using stochastic storm generation (Figure 7, 9 and 10).

4.2 The role of a critical shear stress for latitudinal trends in topography

Increasing values of critical shear stress dampens the magnitude of the latitudinal trends of elevation (Figure 7), as fewer storms are large enough to generate erosion (Figure 20). This is consistent with previous findings that only larger storm events cause the most geomorphic work [*Tucker and Bras, 2000; Tucker, 2004*]. Implementing lower threshold values for erosion increases overall elevation differences (Figure 10). Additionally, lower thresholds increase relative elevation differences and demonstrate a relatively greater geomorphic efficiency in tropical and mid-latitudes (Figure 20). This is because the higher frequency (D:F) of small storms, which accomplish geomorphic work with low thresholds, is greater in the tropical and mid-latitudes than in the sub-tropics (Table 4; Figure 19).

Decreasing critical shear stress means more storms are capable of erosion (Figure 7 and 10). This lowers elevations but has an additional effect of making the tropical latitudes relatively even more efficient than suite 1 (Figure 10). The tropical latitudes are affected more

because of their high D:F ratios. Therefore the result of lowering thresholds is an increase in relative elevation differences along latitude.

Additional insights into how critical shear stress influences topography are apparent with differences in trends between mean and maximum elevations for suite 1 ($K = 1.25e-2$, $\tau_c = 50$; Figure 7). Mean and maximum elevations diverge and hypsometric curves show that elevations relative to the peaks are lower at 45°S (Figure 7; Figure 8). Here, mean precipitation intensity is low (i.e. a lower mean precipitation intensity and a higher D:F ratio; Figure 19). Due to this lower intensity and lower variability in precipitation rates (equation 8), storms that are large enough to overcome the infiltration capacity but not large enough to overcome the critical shear stress (i.e. 50 Pa), and subsequently generate erosion, will cause the headwaters to require larger drainage areas. This low variability precipitation delivered to the landscape at 45°S predicts a lower drainage density as hillslopes dominate the headwaters and lengthen [Tucker and Bras, 2000], which is consistent with higher peaks but lower mean elevations (Figure 7 and 8). The difference in elevation between the headwaters and the ‘peaks’ at 45°S is greater than landscapes at 40 and 50°S (Figure 13a), confirming that there is a lower drainage density and that hillslope processes dominate. Because the mean elevation is much lower than the peaks at 45°S, this suggests that the landscape has adjusted to compensate for the low precipitation variability by increasing relief and lowering drainage density, while D:F ratios play a role in delivering sufficient discharge to the landscapes to drive down elevations lower in the landscape relative to the peaks.

4.3 Orographic influences on efficiency

4.3.1 Orographic differences

Han et al. [2015] couple an orographic precipitation model with a landscape evolution model to test how orographic precipitation affects topography. Their results imply that orographic precipitation has a strong effect on topography and their coupled climate-landscape model provides predictions of how the two systems co-evolve [*Han et al.*, 2015]. Here, I provide measures of geomorphic efficiency due to observed orographic precipitation. Results from across-orogen runs (Figure 12) show the importance of across-orogen precipitation differences and their relationship with latitude. For example, large differences in elevation occur at 25°S where climate varies heavily from West to East (Figure 12). Small differences in elevation occur near the equator (10°S) where climate is rather constant across the orogen (Figure 11 and 12; Table 5).

The gradient in geomorphic efficiency across the orogen changes with latitude and is dependent on the differences in the intensity and D:F ratios. Towards the equator (10°S), low precipitation variability and moderate to high intensity produce lower and constant elevations across the orogen (Figure 11 and 12). Here, geomorphic efficiency is high and constant across the orogen. Latitudes within the Altiplano (25°S) with variable precipitation and D:F ratio across the orogen produce large elevation differences (Figure 12; Table 5). Here, climate produces a gradient in geomorphic efficiency with low efficiency in the West and higher efficiency in the East (Figure 12). Latitudes receiving moderate ranges of intensities and D:F ratios across the orogen (i.e. 20, 30, 45 and 50°S) show moderate gradients in elevation and geomorphic efficiency (Figure 11 and 12). At 20 and 30°S, geomorphic efficiency is lower in the West and increases to the East (Figure 12). This trend follows an increasing West to East

D:F ratio (Figure 11) that generates a decreasing trend in elevations from West to East (Figure 12). This elevation trend is due to an increase in storm duration and intensity West to East, while the overall range in D:F and intensity controls the range in elevation (Figure 11). At 45 and 50°S, an increasing East to West intensity and D:F ratio (Figure 11) generates lower elevations in the West that increase to the East while geomorphic efficiency decreases to the East (Figure 12).

There is a strong latitudinal dependence of orographic precipitation's affect on geomorphic efficiency. Variation in orographic precipitation is capable of generating significant differences in geomorphic efficiency and maximum elevations across the orogen (Figure 12). Differences in elevation due to orographic effects are latitude dependent and the geomorphic efficiency varies heavily at the subtropics (25°S), moderately at the mid and upper-mid latitudes (30, 45 and 50°S), and little at the tropical latitudes (10°S; Figure 12). These findings signify the dependence of the magnitude and variation of orographic precipitation with latitude. Geomorphic efficiency, then, becomes a function of orographic effects in addition to a function of latitude (Figure 12). The effects of orographic precipitation with latitude may be apparent in the modern distribution of the Andes as cross-range asymmetry matches well with my modeled geomorphic efficiency [*Montgomery et al.*, 2001].

4.3.2 Infiltration differences

Infiltration provides an additional buffer to a landscape. This is most apparent for the climate statistics in the upper-mid latitudes (45 and 50°S) for suites using an infiltration rate (suite 1) and suites with an infiltration rate set to zero (suite 8; Figure 7). Where the two trends diverge (45 and 50°S), efficiency increases with a decrease in infiltration rate as a

larger number of storms generate erosion (Figure 7). Such findings support the notion that infiltration provides an additional buffer to climate. It is possible that in some scenarios a storm intensity could be high enough that it would exceed the erosion threshold, but because of the existence of infiltration, the reduced run-off results in discharges that are below the erosion threshold. When infiltration is set to zero, these storms then become erosive. (Figure 7). Landscapes exposed to more overland flow and erosion adjust their slopes to compensate for the increased discharge (Figure 14). This suggests that landscapes with greater infiltration rates are more susceptible to changes in precipitation variability, as their slopes are not exposed to the larger number of storms [i.e. *Tucker and Bras, 2000*].

Additional evidence to support infiltration rates buffering a landscape from erosion comes with the observation that maximum elevations are more constant for the no infiltration case (suite 8; Figure 7). Excluding 20 and 25°S, the range in maximum elevations decreases from suite 1 to suite 8 with the decrease in infiltration (Figure 7). The lower range of elevations shows that the range of precipitation intensities that was able generate a larger diversity of geomorphic efficiency for suite 1 would now need to be larger to generate the same differences in elevations when there is no infiltration. Precipitation intensity, therefore, may play less of a role with no infiltration rate.

The length of the storms dominates landscapes with no infiltration rate. In such cases, low precipitation intensity can be accommodated with a large D:F ratio (Figure 7 and 19). For example, large intensities at 30 and 35°S drive elevations down when infiltration is turned on while small intensities and larger D:F values at 45 and 50°S drive elevations up (Figure 7 and 19). When infiltration is turned off, elevations at 30 and 35°S increase because D:F ratios are low and storm and inter-storm duration become more important. Elevations at 45 and 50°S

decrease because D:F ratios are larger and more storm intensities are capable of generating geomorphic work (Figure 7 and 19).

In addition to having a buffering effect on maximum elevations, the removal of an infiltration rate also results in differences in river channel morphology (Figure 14). Channel morphology may record climatic signals within a landscape [Han *et al.*, 2015]. Because infiltration rates help buffer the landscape from climatic signals, I argue that the difference in certain channel characteristics between suites 1 (infiltration) and 8 (no infiltration) may provide insight into the buffering effects of infiltration. Differences in modeled (S_m) to threshold slope (S_t) ratios between suites 1 and 8 provide the basis for this discussion (Figure 16). Because $S_m:S_t$ values are based off mean precipitation and discharge values (equations 12, 13 and 15), values of $S_m:S_t$ less than one represent locations where events greater than the mean discharge will dominate the erosion signal, consistent with previous work [Tucker, 2004; Tucker and Bras, 2000]. A value greater than one suggests that the frequent smaller events are more important. A greater number of $S_m:S_t$ values below the 1:1 line when the infiltration rate is zero showing that for the most part, threshold slopes (S_t) are larger than modeled slopes (Figure 16b). Because S_t is a function of mean discharge (equation 15), this suggests that the mean discharge does not erode the bed, with the exception of 25°S. Mean discharge rates for suites 1 and 8 are indistinguishably similar and slope ratios are more varied for suite 1 where landscapes have an infiltration rate (Figure 16a). The larger variation is likely an artifact of the timestep assumptions – I increase storm and inter-storm durations to minimize computation time. Additionally, a significant number of slopes reside at or above the 1:1 line. Therefore, a greater number of modeled slopes within landscapes with an infiltration rate are larger than threshold slopes suggesting that the implemented infiltration

rate buffers or protects landscapes from precipitation intensities that are less than the infiltration rate.

4.4 Comparison with modern topography

There are also some key similarities between modeled and modern topography. Modeled elevation trends show maximum elevations at 25°S (Figures 7 and 9) and observations in the Andes show maximum elevations at 27°S (Figure 1). Lower elevations are located between 5 and 10°S for all model runs (Figures 7 and 9) and observations (Figure 1), likely a reflection of the frequent intense weather systems that occur in the tropics (Figure 19).

Differences are to be expected, as the model set up does not capture variations in tectonics and lithology along the Andes. For instance, I assume rock type uniformity with the constant rock erodibility coefficient, K , within each suite. I also assume a uniform and constant rock uplift rate across latitudes and suites. Uplift rates for the Andes range from 0.2 to an upward limit of 3 mm/yr [*Gregory-Wodzicki, 2000; Benjamin et al., 1987*].

Although the simplified case sets a reasonable uplift rate (0.5 mm/yr), it is important to ask what differences in rock-uplift would be necessary to erase the differences in elevation output by the climatic-controlled runs. This would provide insight into the importance of climate vs. rock-uplift in generating topographic trends with latitude. By establishing uplift rates necessary to erase these elevation differences, I can then evaluate if the increases in uplift create feasible rock uplift rates to explain the modeled differences in elevation.

To test these questions, I set up additional model runs using climate data from 10°S, increasing the uplift rate sequentially for each model run to ‘match’ the maximum elevation. I use climatic inputs from 10°S because it produces the lowest maximum elevations for suites 2 and 3 and the second lowest maximum elevations for suite 1 (Figure 7). I run each model for

60 Myr and increase the uplift rate with each run from the original uplift rate of 0.5 mm/yr. I record the maximum elevations at dynamic equilibrium to compare with suites 1-3. Figure 21 shows the maximum elevations from the landscapes in dynamic equilibrium with the incremental increases in uplift rate. The y-axis is normalized by the maximum elevation at 10°S from suite 1 (1.98 km), suite 2 (155.12 m) and suite 3 (61 m) to show the increase in elevation resulting from each increase in uplift (Figure 21).

The results are shown in Figure 21. Fitting linear regressions to extrapolate beyond the model analysis (arrows), I project increases in uplift rate of 27.1x (suite 1), 21.8x (suite 2) and 22.6x (suite 3), where x is the original uplift rate of 0.5 mm/yr (Figure 21). These increases result in uplift rates of 13.6 mm/yr (suite 1), 10.9 mm/yr (suite 2) and 11.3 mm/yr (suite 3), and reveal the rates required to produce similar elevations across the latitudes. Therefore, a range of a minimum uplift rate of 0.5 mm/yr and a maximum of 20-30 times the minimum is required to produce a ~2.6 fold difference in maximum elevation (for suite 1), ~7 fold difference in maximum elevation (for suite 2) and ~21 fold difference in maximum elevation (for suite 3).

Typical variation in uplift rates along the Andes are within an order of magnitude and are much less than the predictions [*Benjamin et al.*, 1987; *Gregory-Wodzicki*, 2000]. The findings suggest that uplift alone cannot explain the latitudinal trends. Climate, and the role of stochastic storm distributions, is important for understanding latitudinal trends of topography in the Andes.

Chapter 5: Conclusion

I demonstrate a first order control of climate on erosion processes and topography. Geomorphic efficiency varies across the orogen and the degree of this variation is a function of latitude as a result of differences in storm intensity, duration, and inter-storm duration. Drier latitudes with high precipitation variability produce a large range in modeled elevations across the orogen while latitudes with low precipitation variability produce consistent elevations across the orogen. Maximum elevation trends produced using stochastically generated storm differ significantly from trends produced using MAP. Infiltration and critical shear stress thresholds act as buffers that act along the latitudinal and climate gradients. Based on the model results, I conclude that complexities associated with stochastic storms, critical shear stress, infiltration associated with differences in landscapes in addition to previous work using MAP could help explain the differing conclusions on the climatic control on topography and erosion.

References

- Avouac, J. P., and E. B. Burov (1996), Erosion as a driving mechanism of intracontinental mountain growth, *J. Geophys. Res. Solid Earth*, *101*(B8), 17747–17769, doi:10.1029/96JB01344.
- Beaumont, C., P. Fullsack, and J. Hamilton (1992), Erosional control of active compressional orogens, in *Thrust Tectonics*, edited by K. R. McClay, pp. 1–18, Springer Netherlands.
- Benjamin, M. T., N. M. Johnson, and C. W. Naeser (1987), Recent rapid uplift in the Bolivian Andes: Evidence from fission-track dating, *Geology*, *15*(7), 680–683, doi:10.1130/0091-7613(1987)15<680:RRUITB>2.0.CO;2.
- Bookhagen, B., R. C. Thiede, and M. R. Strecker (2005), Abnormal monsoon years and their control on erosion and sediment flux in the high, arid northwest Himalaya, *Earth Planet. Sci. Lett.*, *231*(1–2), 131–146, doi:10.1016/j.epsl.2004.11.014.
- Brozović, N., D. W. Burbank, and A. J. Meigs (1997), Climatic Limits on Landscape Development in the Northwestern Himalaya, *Science*, *276*(5312), 571–574, doi:10.1126/science.276.5312.571.
- Buffington, J. M., and D. R. Montgomery (1997), A systematic analysis of eight decades of incipient motion studies, with special reference to gravel-bedded rivers, *Water Resour. Res.*, *33*(8), 1993–2029, doi:10.1029/96WR03190.
- Burbank, D. W., A. E. Blythe, J. Putkonen, B. Pratt-Sitaula, E. Gabet, M. Oskin, A. Barros, and T. P. Ojha (2003), Decoupling of erosion and precipitation in the Himalayas, *Nature*, *426*(6967), 652–655, doi:10.1038/nature02187.
- Dadson, S. J. et al. (2003), Links between erosion, runoff variability and seismicity in the Taiwan orogen, *Nature*, *426*(6967), 648–651.
- Decker, M., M. A. Brunke, Z. Wang, K. Sakaguchi, X. Zeng, and M. G. Bosilovich (2011), Evaluation of the Reanalysis Products from GSFC, NCEP, and ECMWF Using Flux Tower Observations, *J. Clim.*, *25*(6), 1916–1944, doi:10.1175/JCLI-D-11-00004.1.
- Eagleson, P. S. (1978), Climate, soil, and vegetation: 1. Introduction to water balance dynamics, *Water Resour. Res.*, *14*(5), 705–712, doi:10.1029/WR014i005p00705.
- Egholm, D. L., S. B. Nielsen, V. K. Pedersen, and J.-E. Lesemann (2009), Glacial effects limiting mountain height, *Nature*, *460*(7257), 884–887, doi:10.1038/nature08263.
- European Centre for Medium-Range Weather Forecasts (2009), ERA-Interim Project, <http://dx.doi.org/10.5065/D6CR5RD9>, Research Data Archive at the National Center for Atmospheric Research, Computational and Information Systems Laboratory, Boulder, Colo. (Updated Monthly.) Accessed 09 09 2014.

- Ferrier, K. L., K. L. Huppert, and J. T. Perron (2013), Climatic control of bedrock river incision, *Nature*, 496(7444), 206–209, doi:10.1038/nature11982.
- Gregory-Wodzicki, K. M. (2000), Uplift history of the Central and Northern Andes: A review, *Geol. Soc. Am. Bull.*, 112(7), 1091–1105, doi:10.1130/0016-7606(2000)112<1091:UHOTCA>2.0.CO;2.
- Han, J., N. M. Gasparini, and J. P. L. Johnson (2015), Measuring the imprint of orographic rainfall gradients on the morphology of steady-state numerical fluvial landscapes, *Earth Surf. Process. Landf.*, n/a–n/a, doi:10.1002/esp.3723.
- Howard, A. D., and G. Kerby (1983), Channel changes in badlands, *Geol. Soc. Am. Bull.*, 94(6), 739–752, doi:10.1130/0016-7606(1983)94<739:CCIB>2.0.CO;2.
- Jeffery, M. L., B. J. Yanites, C. J. Poulsen, and T. A. Ehlers (2014), Vegetation-precipitation controls on Central Andean topography, *J. Geophys. Res. Earth Surf.*, 2013JF002919, doi:10.1002/2013JF002919.
- Leeder, M. R., T. Harris, and M. J. Kirkby (1998), Sediment supply and climate change: implications for basin stratigraphy, *Basin Res.*, 10(1), 7–18, doi:10.1046/j.1365-2117.1998.00054.x.
- Leopold, L., and T. Maddock (1953), The Hydraulic Geometry of Stream Channels and Some Physiographic Implications, *Y Rep.*
- Maher, K., and C. P. Chamberlain (2014), Hydrologic Regulation of Chemical Weathering and the Geologic Carbon Cycle, *Science*, 343(6178), 1502–1504, doi:10.1126/science.1250770.
- Mitchell, S., and D. Montgomery (2006), Influence of a glacial buzzsaw on the height and morphology of the Cascade Range in central Washington State, USA, *Quat. Res.*, 65(1), 96–107, doi:10.1016/j.yqres.2005.08.018.
- Montgomery, D. R., G. Balco, and S. D. Willett (2001), Climate, tectonics, and the morphology of the Andes, *Geology*, 29(7), 579–582.
- Ouimet, W. B., K. X. Whipple, and D. E. Granger (2009), Beyond threshold hillslopes: Channel adjustment to base-level fall in tectonically active mountain ranges, *Geology*, 37(7), 579–582, doi:10.1130/G30013A.1.
- Raymo, M. E., and W. F. Ruddiman (1992), Tectonic forcing of late Cenozoic climate, *Nature*, 359(6391), 117–122, doi:10.1038/359117a0.
- Riebe, C. S., J. W. Kirchner, D. E. Granger, and R. C. Finkel (2001), Minimal climatic control on erosion rates in the Sierra Nevada, California, *Geology*, 29(5), 447–450, doi:10.1130/0091-7613(2001)029<0447:MCCOER>2.0.CO;2.
- Roe, G. H. (2005), Orographic Precipitation, *Annu. Rev. Earth Planet. Sci.*, 33, 645–671.

- Shields, A. (1936), Anwendung der Ähnlichkeits-Mechanik und der Turbulenzforschung auf die Gletscherbewegung, *Preuss. Vers. Für Wasserbau Schiffbau*, 26, 524–526.
- Torres, M. A., A. J. West, and G. Li (2014), Sulphide oxidation and carbonate dissolution as a source of CO₂ over geological timescales, *Nature*, 507(7492), 346–349, doi:10.1038/nature13030.
- Tucker, G., S. Lancaster, N. Gasparini, and R. Bras (2001), The channel-hillslope integrated landscape development model (CHILD), in *Landscape erosion and evolution modeling*, pp. 349–388, Springer.
- Tucker, G. E. (2004), Drainage basin sensitivity to tectonic and climatic forcing: implications of a stochastic model for the role of entrainment and erosion thresholds, *Earth Surf. Process. Landf.*, 29(2), 185–205, doi:10.1002/esp.1020.
- Tucker, G. E., and R. L. Bras (2000), A stochastic approach to modeling the role of rainfall variability in drainage basin evolution, *Water Resour. Res.*, 36(7), 1953–1964.
- Walker, J. C. G., P. B. Hays, and J. F. Kasting (1981), A negative feedback mechanism for the long-term stabilization of Earth's surface temperature, *J. Geophys. Res. Oceans*, 86(C10), 9776–9782, doi:10.1029/JC086iC10p09776.
- Whipple, K. X., and G. E. Tucker (1999), Dynamics of the stream-power river incision model: Implications for height limits of mountain ranges, landscape response timescales, and research needs, *J. Geophys. Res. Solid Earth*, 104(B8), 17661–17674, doi:10.1029/1999JB900120.
- Whipple, K. X., E. Kirby, and S. H. Brocklehurst (1999), Geomorphic limits to climate-induced increases in topographic relief, *Nature*, 401(6748), 39–43, doi:10.1038/43375.
- Wobus, C., K. X. Whipple, E. Kirby, N. Snyder, J. Johnson, K. Spyropolou, B. Crosby, and D. Sheehan (2006), Tectonics from topography: Procedures, promise, and pitfalls, *Geol. Soc. Am. Spec. Pap.*, 398, 55–74, doi:10.1130/2006.2398(04).
- Zachos, J. C., G. R. Dickens, and R. E. Zeebe (2008), An early Cenozoic perspective on greenhouse warming and carbon-cycle dynamics, *Nature*, 451(7176), 279–283, doi:10.1038/nature06588.

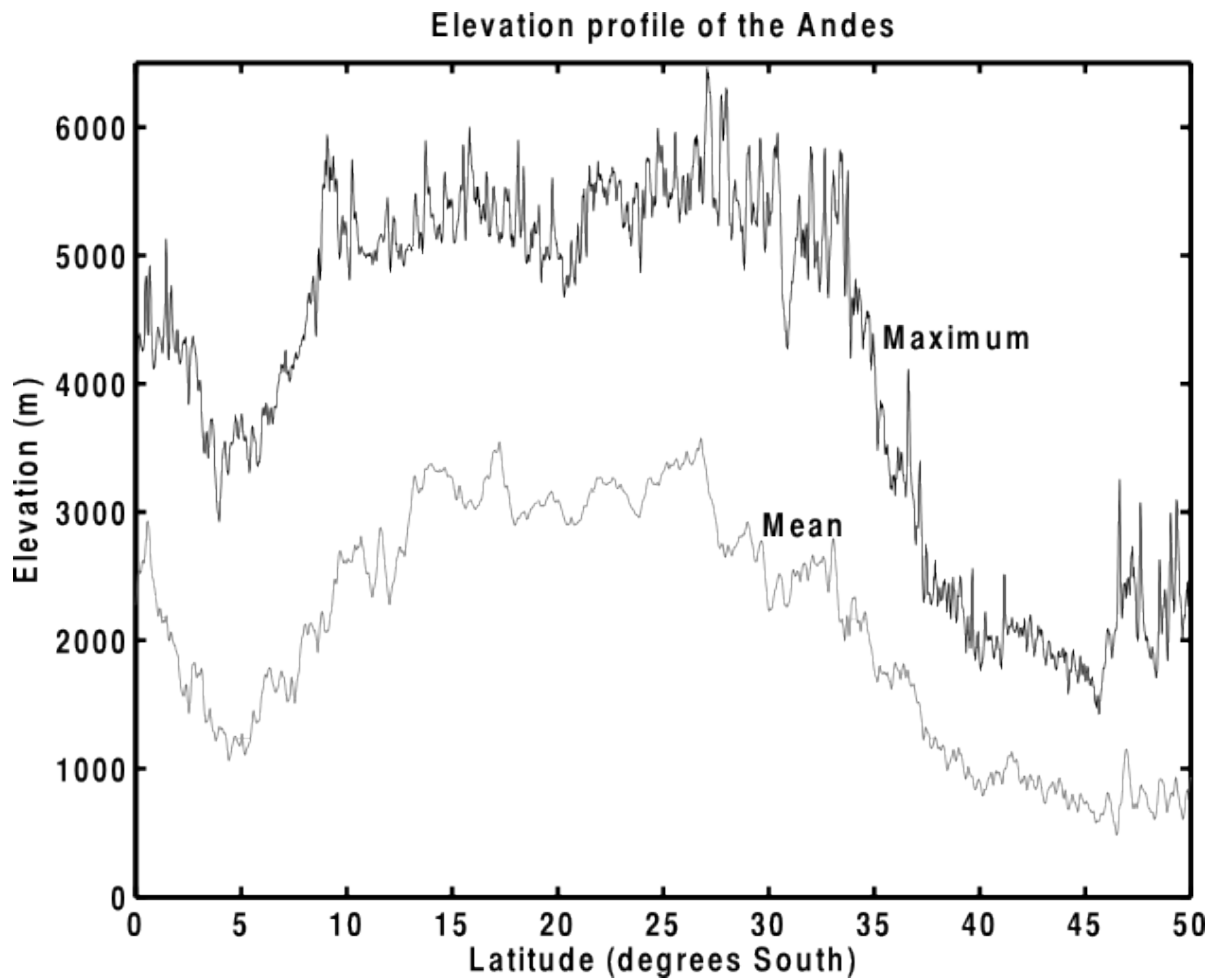


Figure 1: Elevation profiles of the North (a) and South (b) American Cordillera. Maximum elevations (black lines) and mean elevations (gray lines) show lower elevations toward the equator, high elevations between 10 and 40°S and a strong decrease toward the poles beginning at 30°S to 40°S.

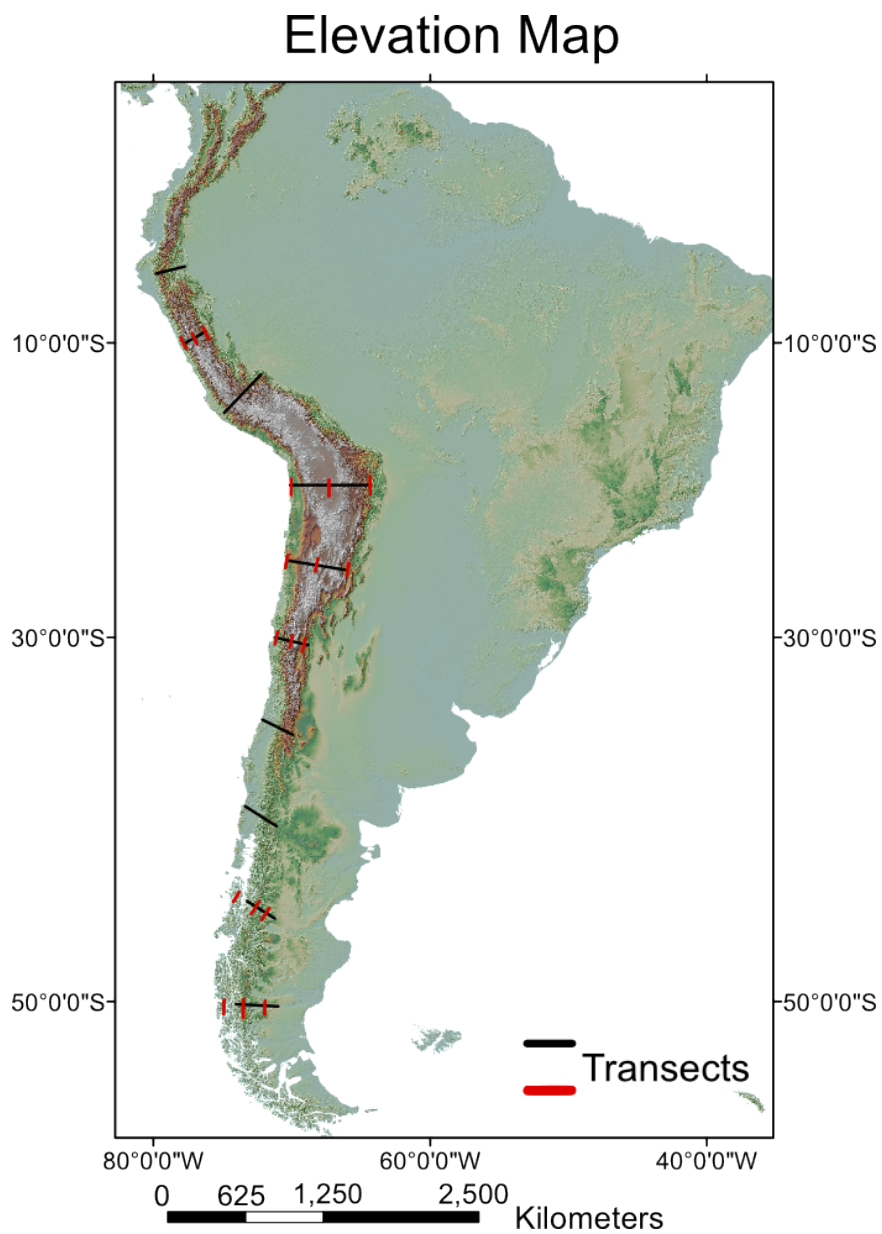


Figure 2: Elevation map of the Andes. 10 black lines represent locations where we extracted climate data for each run. 18 red lines represent our orographic runs for latitudes 10°S, 20°S, 25°S, 30°S, 45°S and 50°S.

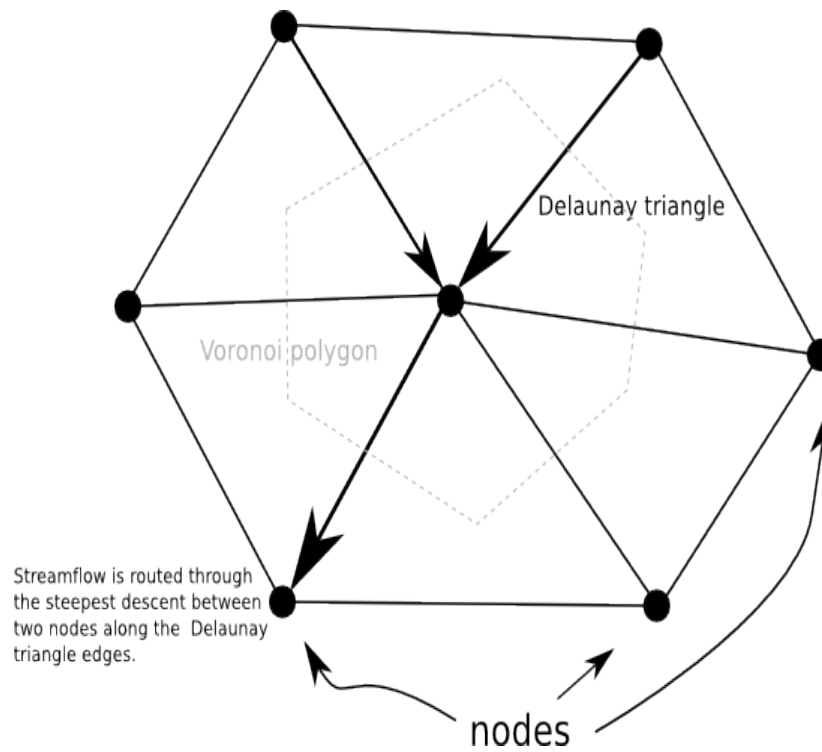


Figure 3: CHILD triangular mesh setup. Nodes track elevation changes, water is routed along the Delaunay triangle edges and the area of each node is a finite entity represented by a Voronoi polygon (or cell). Each cell is assumed to contain a channel. Arrows represent the direction of flow.

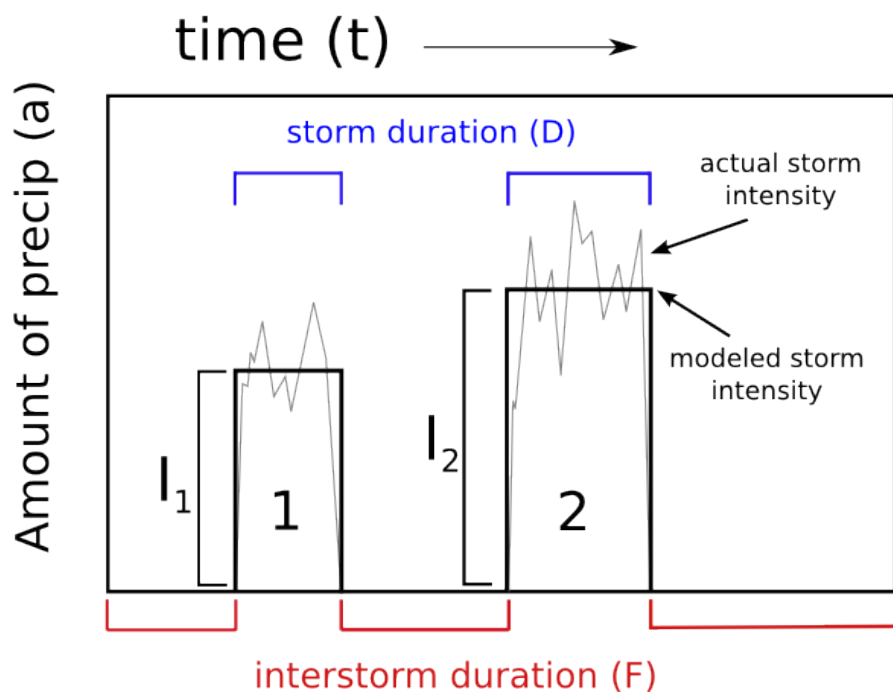


Figure 4: Graphical representation of storm statistics. I = intensity, D = duration, and F = inter-storm duration. Two storms are represented here with an actual storm intensity (gray lines) while CHILD represents storms with a uniform precipitation intensity (black bar). The mean storm duration (\bar{D}) is the average time that it is raining. The mean inter-storm duration (\bar{F}) is the average time it is not raining. The mean intensity (\bar{I}) is the total amount of rain over the time it was precipitated.

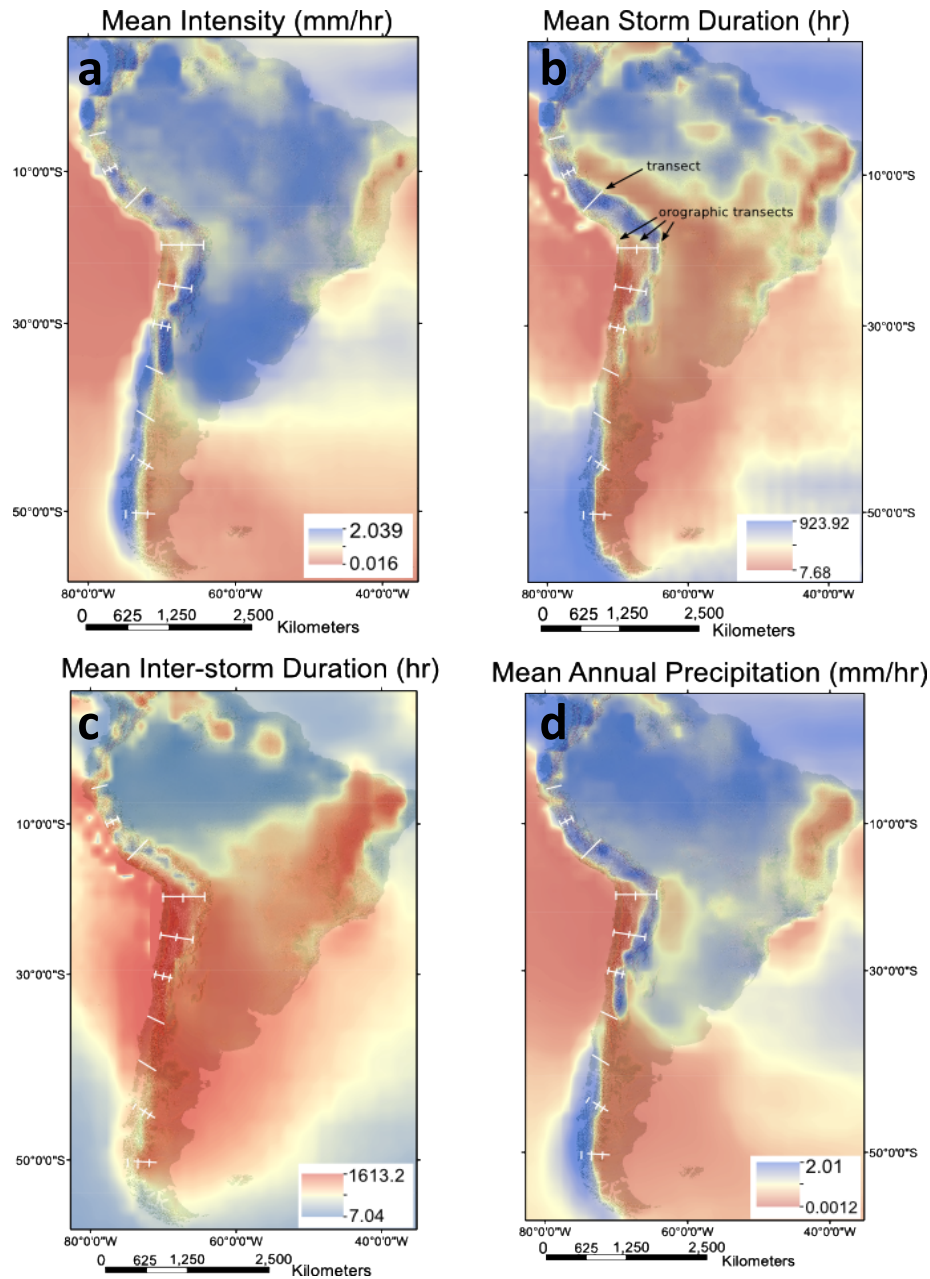


Figure 5: Storm statistic maps. These are generated using 31-year, 6-hourly and global reanalysis data from the European Centre of Medium-Range Weather Forecasts. Statistics are averaged over the 31-year length of the data set. (a) Mean storm intensity, (b) mean storm duration and (c) mean inter-storm duration are extracted and averaged along 10 transects and used as climate input parameters into a landscape evolution model as a stochastic representation of actual climate. Wetter areas are shown in blue, representing larger mean intensities (a), longer mean storms durations (b), and shorter mean inter-storm durations (c). Drier areas are shown in red.

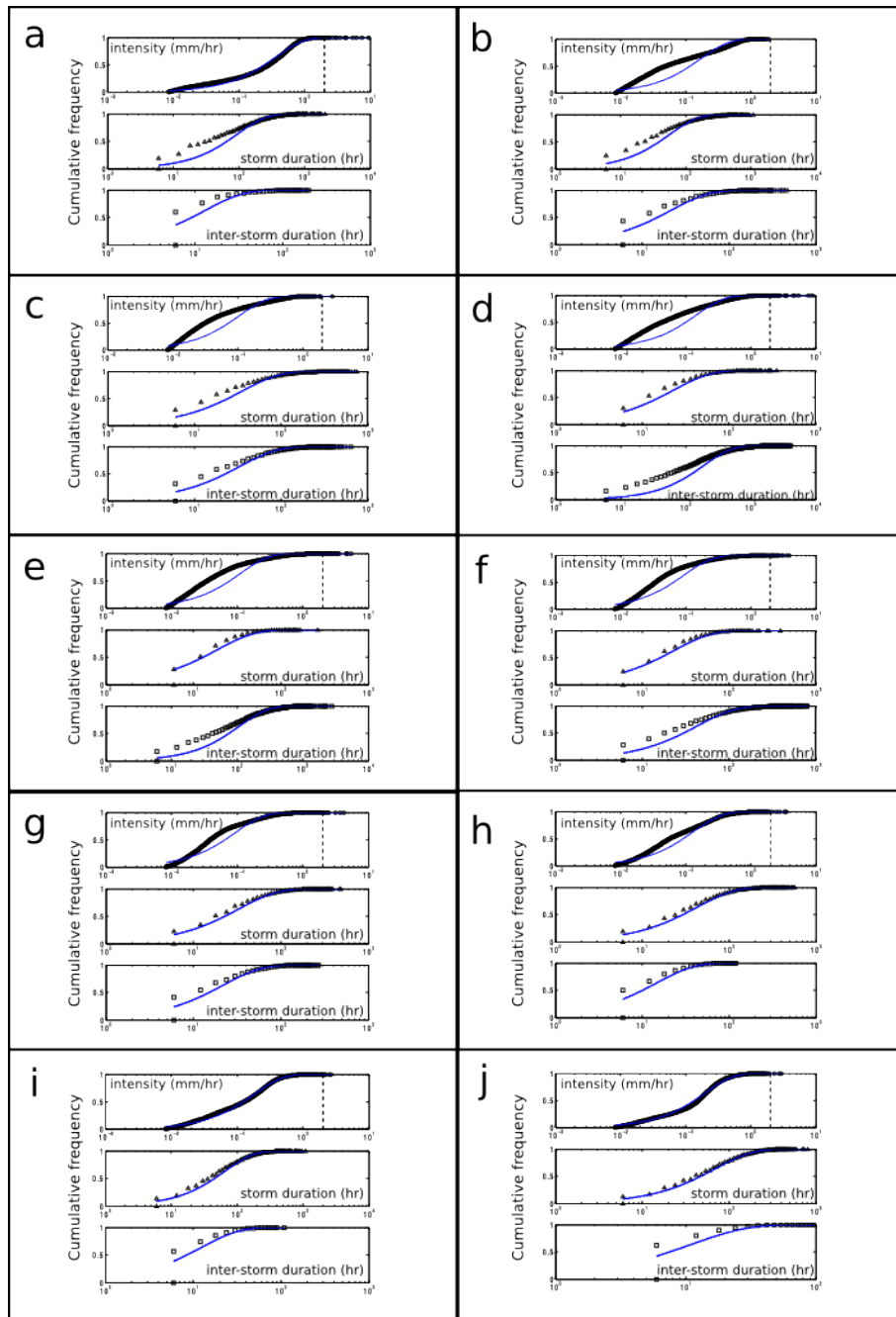


Figure 6: Cumulative distribution plot of intensity (circles; top of each box), duration (triangles; middle of each box) and inter-storm duration (squares; bottom of each box) calculated using 31-year global reanalysis data from European Centre of Medium-Range Weather Forecasts (ECMWF, 2009). Data is extracted over the 10 transects along the Andes (Figure 2): (a) 5°S, (b) 10°S, (c) 15°S, (d) 20°S, (e) 25°S, (f) 30°S, (g) 35°S, (h) 40°S, (i) 45°S and (j) 50°S. Blue lines represent cumulative probability density functions calculated from equations 6, 7 and 8. Vertical dashed lines in the intensity plots represent the infiltration rate. These are used to generate distributions for storms within the CHILD model and provide good approximations for actual distributions.

Suite	τ_c	K	Infiltration	Climate	Section	Δ from suite 1
1	50	1.25E-02	17.5	stochastic	Baseline	control
2	5	1.25E-02	17.5	stochastic	Baseline	} decrease τ_c
3	0.5	1.25E-02	17.5	stochastic	Baseline	
4	5	1.00E-05	0	MAP	Sensitivity	
5	0.5	1.00E-05	0	MAP	Sensitivity	
6	5	2.80E-03	17.5	stochastic	Sensitivity	} decrease K
7	0	2.50E-03	17.5	stochastic	Sensitivity	
8	50	9.00E-05	0	stochastic	Sensitivity	decrease inf.
9	50	9.00E-05	0	stochastic	Orographic	transect locations

Table 1: Naming scheme and distinguishing input parameters. Suite 1 is the control run. I test a decrease in critical shear stress (τ_c) to 5 Pa (Suite 2) and 0.5 Pa (Suite 3). I test the sensitivity to difference climate regimes in Suites 4 and 5 by using MAP. Here, I decrease infiltration and rock erodibility so reasonable elevations are generated. Suites 6 and 7 test the sensitivity to a decrease in rock erodibility (K). Reasonable elevations require a decrease in critical shear stress ($\tau_c = 5$ Pa for Suite 6 and $\tau_c = 0$ Pa for Suite 7). Suite 8 tests a decrease in infiltration rate. Here reasonable elevations require a decrease in rock erodibility (K). Finally, Suite 9 tests orographic precipitation on geomorphic efficiency. Here, I change the locations of the transects to capture climate at different locations relative to the orogen (see Figure 2).

Parameters	Value	Units	Notes
Runtime	60	My	
Output interval	1	My	
Length (X)	100	km	
Width (Y)	100	km	
Node spacing	500	m	
K	varies	$\text{m yr}^{-1} \text{Pa}^{-1}$	rock erodibility coefficient
K_t	1000	$\text{Pa s}^{1/3} \text{m}^{-2/3}$	shear stress (or stream power) coefficient
mt	2/3		bedrock erodibility specific discharge exp
nt	2/3		bedrock erodibility slope expo
P_b	1.50		expo on excess erosion capacity
τ_c	0, 0.5, 5, 50	Pa	critical shear stress (varies)
Uplift rate	5.00E-04	m yr^{-1}	
k_w	10		hydraulic width coefficient
w_s	0.5		hydraulic width exponent
w_b	0.5		hydraulic width exponent
i	0, 17.5	m yr^{-1}	infiltration rate
R_b	13.6	m yr^{-1}	bankful runoff rate

Table 2: Input parameters for model runs.

Input values	Value	Units	Notes
gravity	9.8	m s^{-2}	for grain size calculations
ρ_s	2650	kg m^{-3}	for grain size calculations
ρ_w	1000	kg m^{-3}	for grain size calculations
θ	0.03 - 0.06	unitless	for grain size calculations
D	5.15 - 10.31	cm	grain diameter

Table 3: Input values for grain size calculations

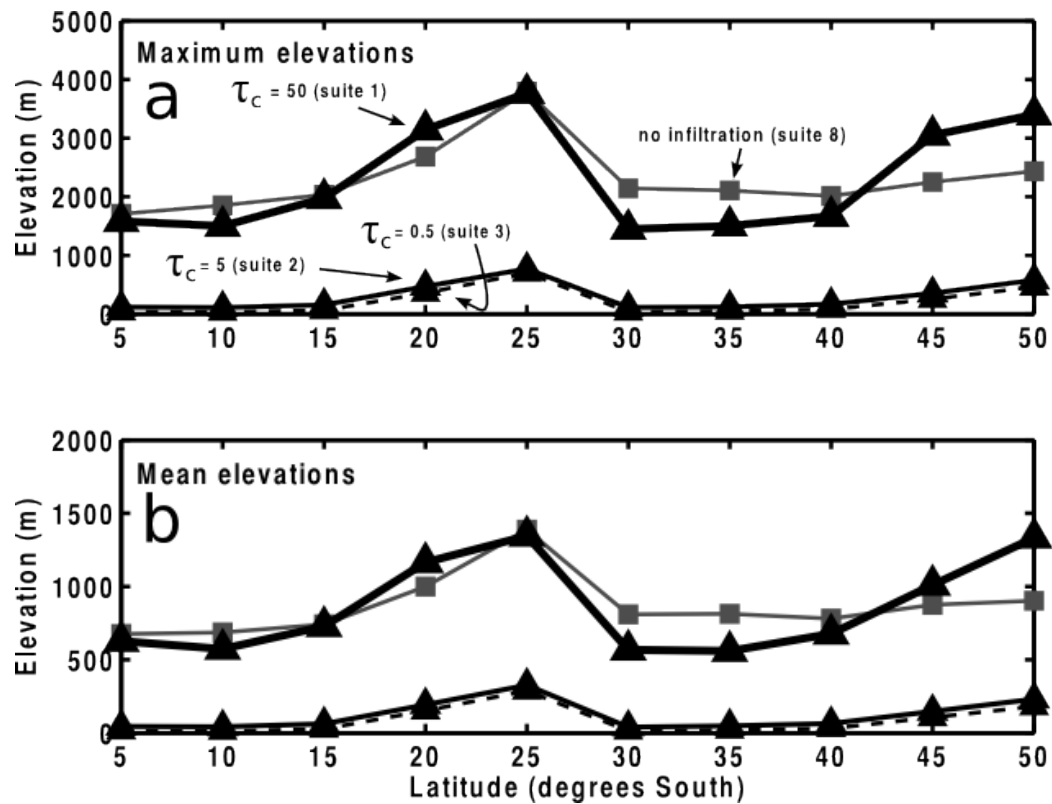


Figure 7: Trends produced by suites 1-3 and 8. Maximum (a) and mean (b) elevations are extracted from 10 steady-state topographies for each suite and plotted against their respective latitude. Solid bold black line with triangles represents elevations from suite 1 ($\tau_c = 50$); Solid thin black line with triangles represents elevations from suite 2 ($\tau_c = 5$); Dashed thin black line with triangles represents elevations from suite 3 ($\tau_c = 0.5$); Dark gray line with squares represents elevations from suite 8 ($\tau_c = 50$ and no infiltration).

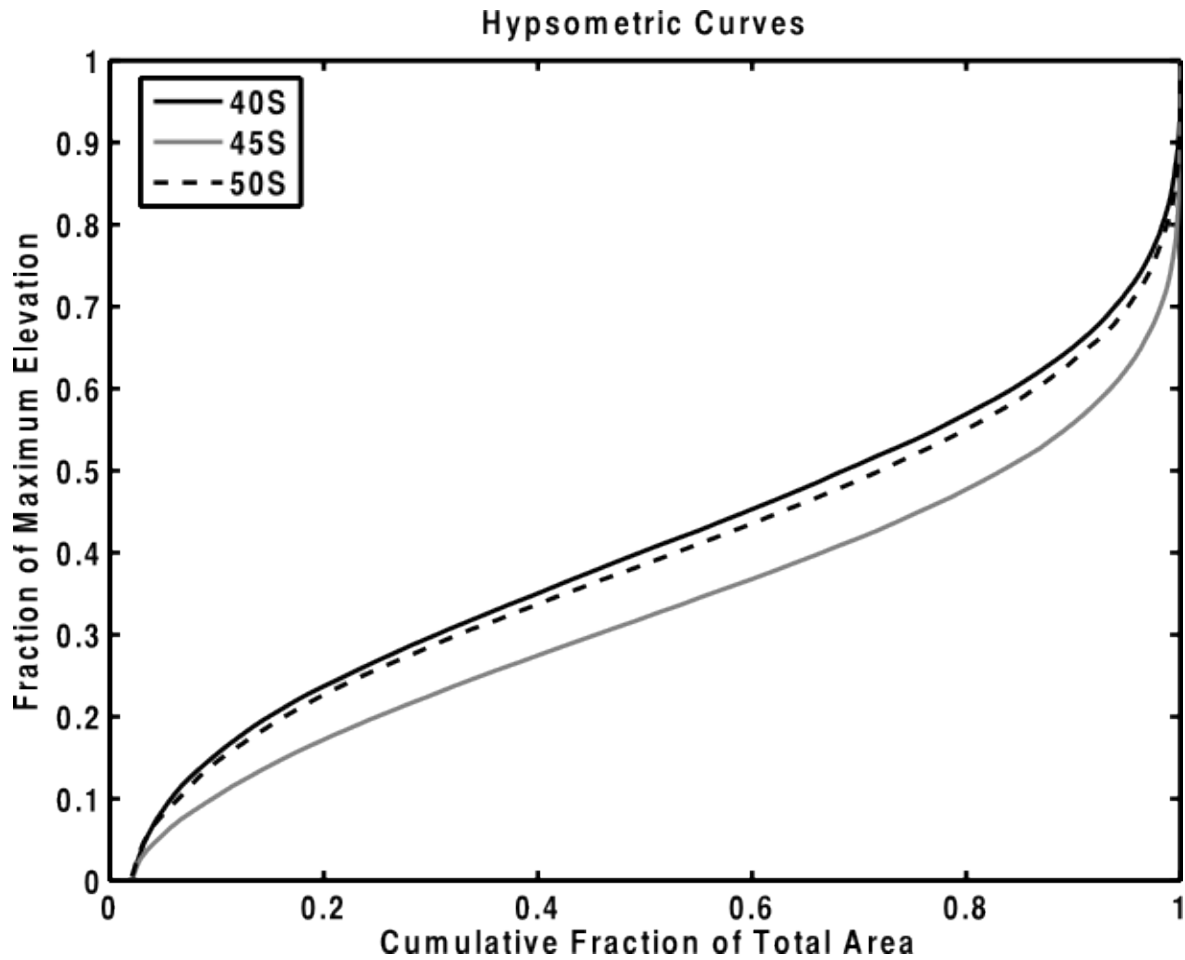


Figure 8: Hypsometric curves for steady state landscapes at 40°S, 45°S and 50°S from suite 1 ($\tau_c=50$; $K= 1.25e-2$). The curve from the landscape at 45°S resides lower than 40°S and 50°S suggesting that a larger fraction of the total area is contained in lower elevations.

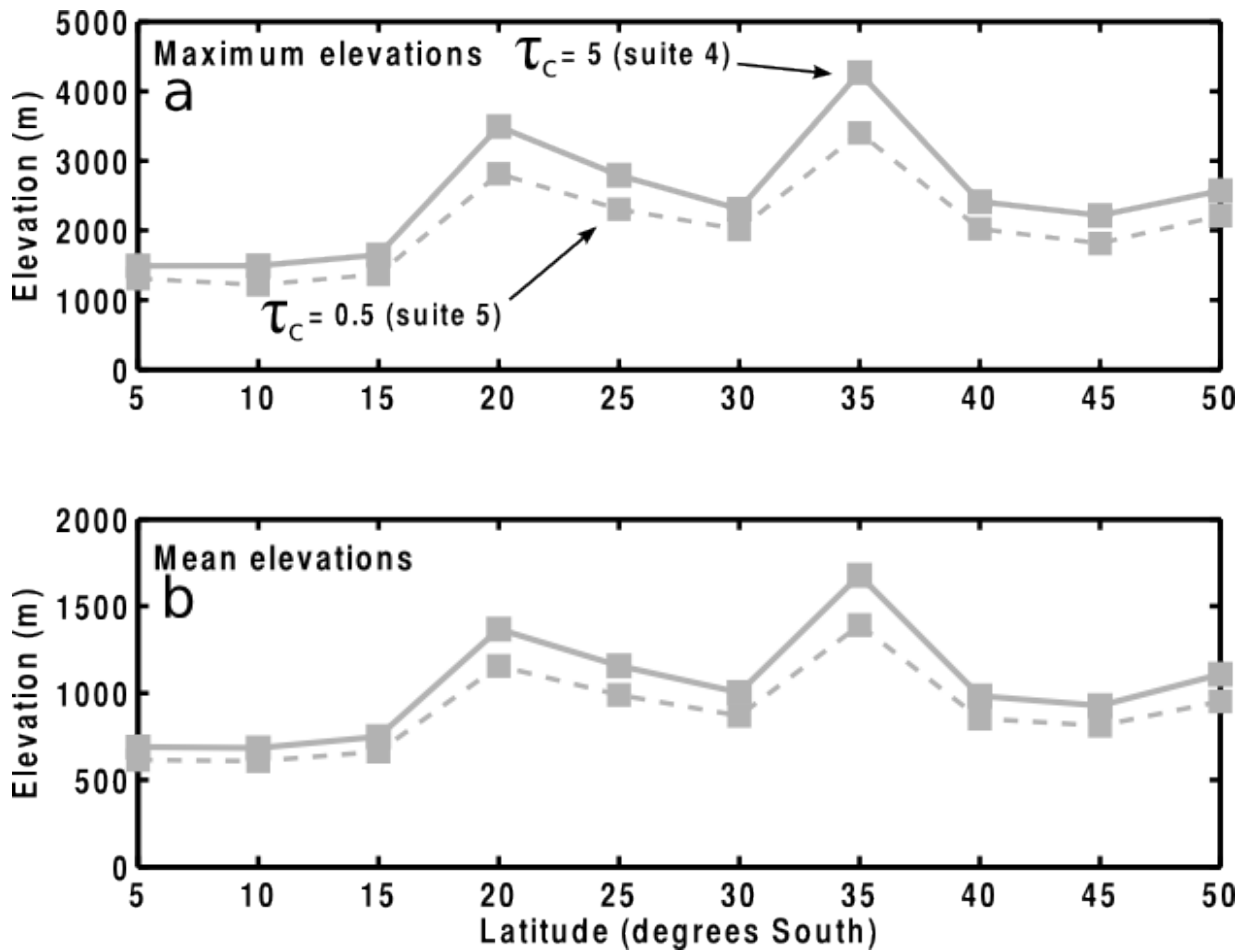


Figure 9: Trends produced by suites 4 and 5. Maximum (a) and mean (b) elevations are extracted from 10 steady-state topographies for each suite and plotted against their respective latitude. Solid gray line with squares represents elevations from suite 4 ($\tau_c = 5$); Dashed gray line with squares represents elevations from suite 5 ($\tau_c = 0.5$).

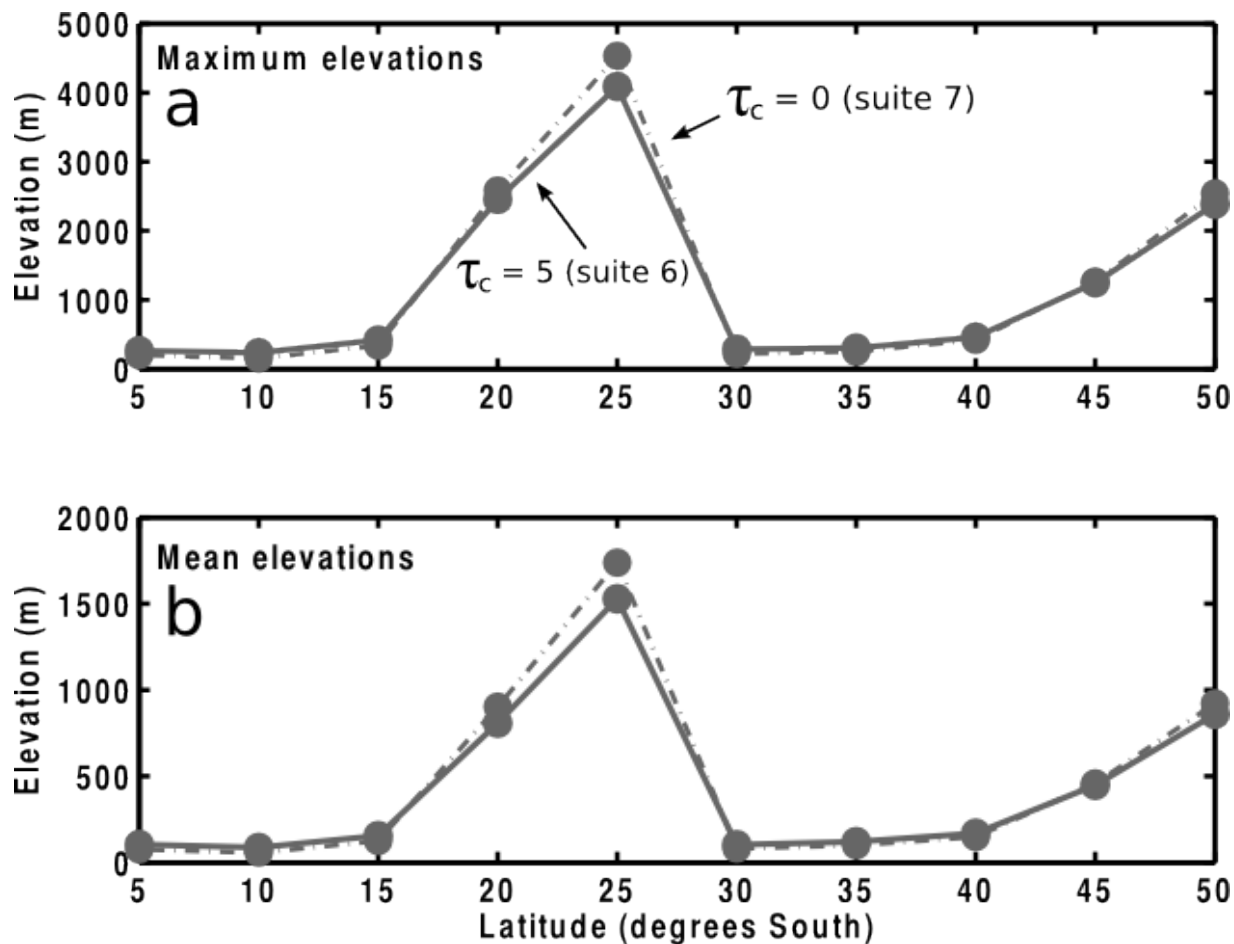


Figure 10: Trends produced by suites 6 and 7. Maximum (a) and mean (b) elevations are extracted from 10 steady-state topographies for each suite and plotted against their respective latitude. Solid gray line with circles represents elevations from suite 6 ($\tau_c = 5$); Dashed gray line with circles represents elevations from suite 7 ($\tau_c = 0$).

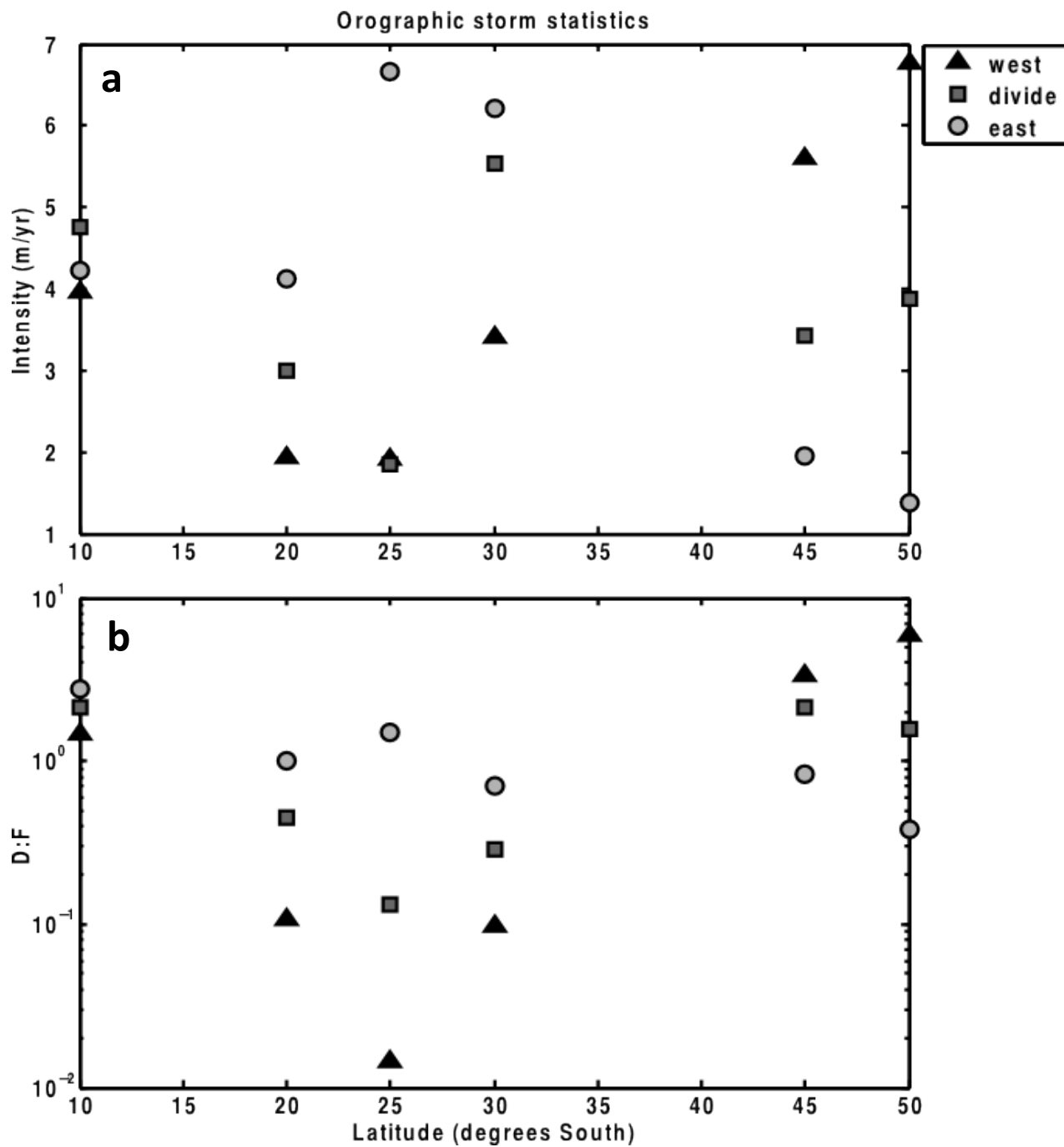


Figure 11: Precipitation inputs for our orographic runs: precipitation intensities (a) and Duration to Inter-storm duration ratios (b). Table 5 shows the classification of variability, magnitude, and range of these values.

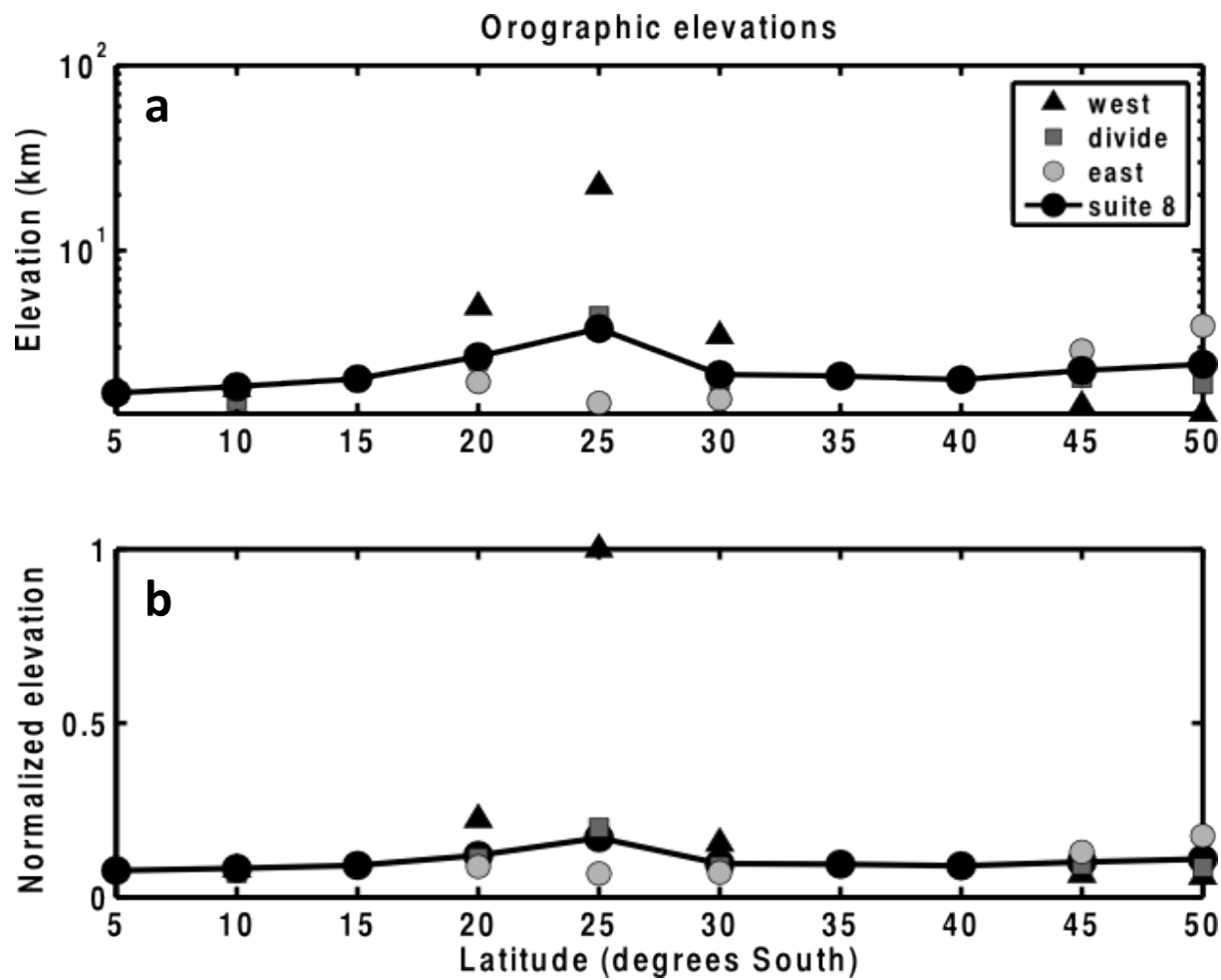


Figure 12: Maximum elevation (a) and relative elevation (b) trends produced by suite 8 and our orographic runs. Elevations are normalized by the maximum elevation at 25°S (b). Triangles represent maximum elevations over the western side, squares are modeled maximum elevations over the divide, and circles are modeled maximum elevations over the east side. All maximum elevations are extracted from modeled landscapes generated using precipitation statistics over the Andes at 10°S, 20°S, 25°S, 30°S, 45°S and 50°S.

Latitude	Intensity (m/yr)	Duration (yrs)	Inter-storm duration (yrs)	MAP (m/yr)	D:F
5	4.05	4.90E-03	2.40E-03	2.84	2.04
10	4.27	5.70E-03	2.60E-03	2.89	2.19
15	3.61	6.90E-03	3.30E-03	2.51	2.09
20	3.07	3.70E-03	1.11E-02	1.19	0.33
25	3.55	3.10E-03	4.01E-02	1.42	0.08
30	5.14	3.20E-03	1.29E-02	1.69	0.25
35	5.13	3.00E-03	1.34E-02	0.98	0.22
40	3.80	4.20E-03	5.90E-03	1.73	0.71
45	2.95	5.20E-03	3.80E-03	1.86	1.37
50	2.78	4.50E-03	4.80E-03	1.50	0.94

Table 4: Mean storm statistic input values for climate parameters in CHLD model for suites 1-8. D:F is the ratio between Duration and Inter-storm duration.

		West	Mid	East	range	magnitude	variability	Direction
10	I	3.96	4.75	4.23	0.78	mod-high	low	N/A
	D	5.43E-03	6.18E-03	5.24E-03				
	F	3.70E-03	2.92E-03	1.91E-03				
	D:F	1.47	2.11	2.75	1.28	high	low	W-E
20	I	1.94	3.00	4.11	2.18	low-mod	moderate	W-E
	D	3.25E-03	3.38E-03	4.59E-03				
	F	3.06E-02	7.47E-03	4.56E-03				
	D:F	0.11	0.45	1.01	0.90	mod-high	moderate	W-E
25	I	1.90	1.85	6.66	4.81	low-high	high	W-E
	D	1.82E-03	2.29E-03	5.55E-03				
	F	1.27E-01	1.72E-02	3.72E-03				
	D:F	0.01	0.13	1.49	1.48	low-high	high	W-E
30	I	3.40	5.54	6.20	2.81	mod-high	moderate	W-E
	D	2.63E-03	3.15E-03	3.77E-03				
	F	2.69E-02	1.09E-02	5.35E-03				
	D:F	0.10	0.29	0.70	0.61	low	low	W-E
45	I	5.60	3.43	1.96	3.64	low-high	high	E-W
	D	1.01E-02	6.32E-03	3.35E-03				
	F	3.04E-03	3.00E-03	4.04E-03				
	D:F	3.32	2.11	0.83	2.49	mod-high	moderate	E-W
50	I	6.77	3.89	1.38	5.39	low-high	high	E-W
	D	1.59E-02	6.30E-03	2.15E-03				
	F	2.72E-03	4.00E-03	5.62E-03				
	D:F	5.85	1.57	0.38	5.47	mod-high	moderate	E-W

Table 5: Mean storm statistics as inputs for climate parameters within CHILD model for our orographic runs (suite 9). I = mean intensity, D = mean storm duration, F = inter-storm duration and D:F is the ratio between storm and inter-storm duration.

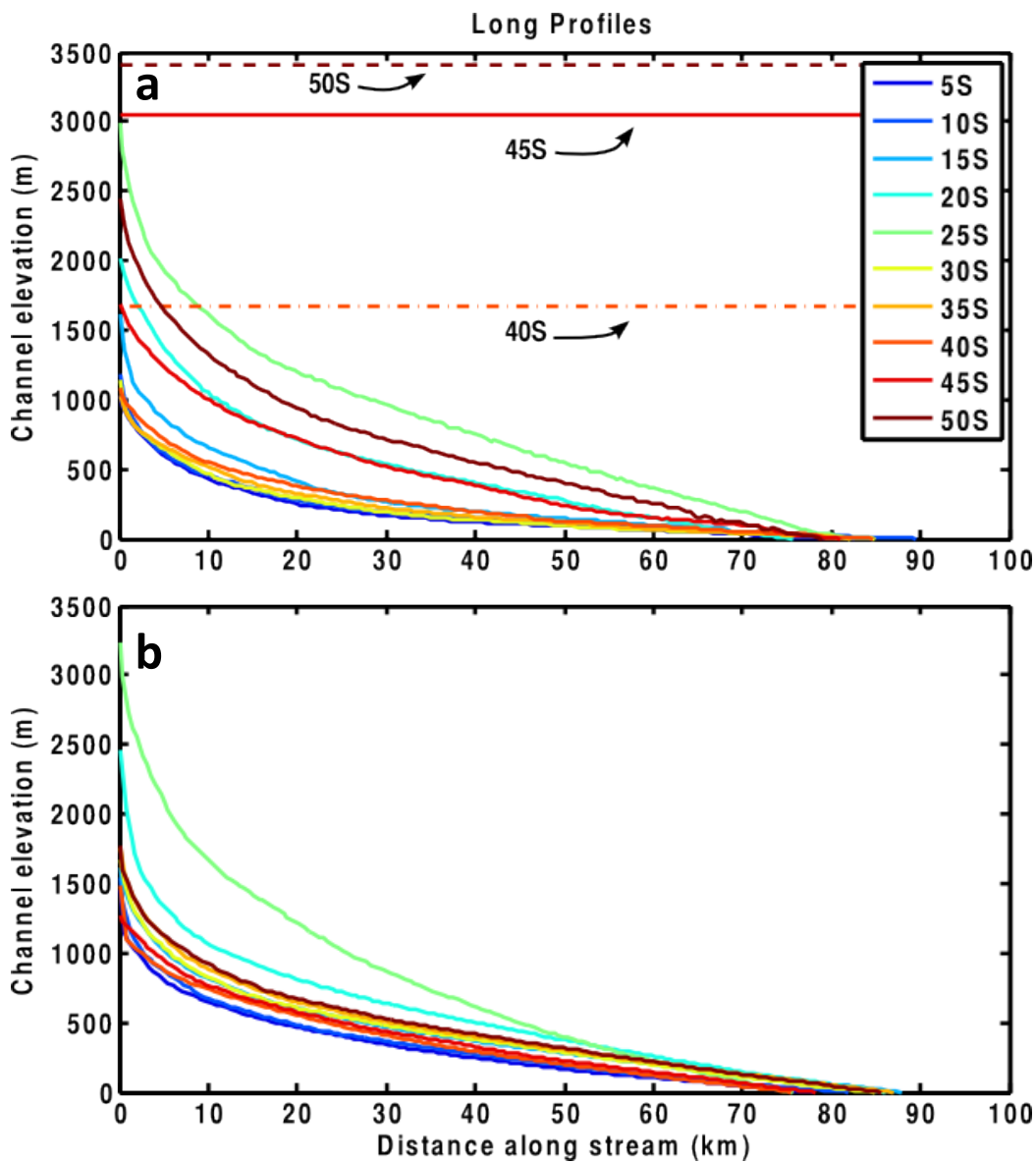


Figure 13: Modeled longitudinal profiles for suites 1 (a) and 8 (b). Elevation data is extracted along the channel profile for each landscape and plotted against the distance from the headwaters. The horizontal lines (a) represent the maximum elevations for landscapes at 40°S, 45°S and 50°S. Notice the large difference in elevation between the headwaters and maximum elevation for 45°S.

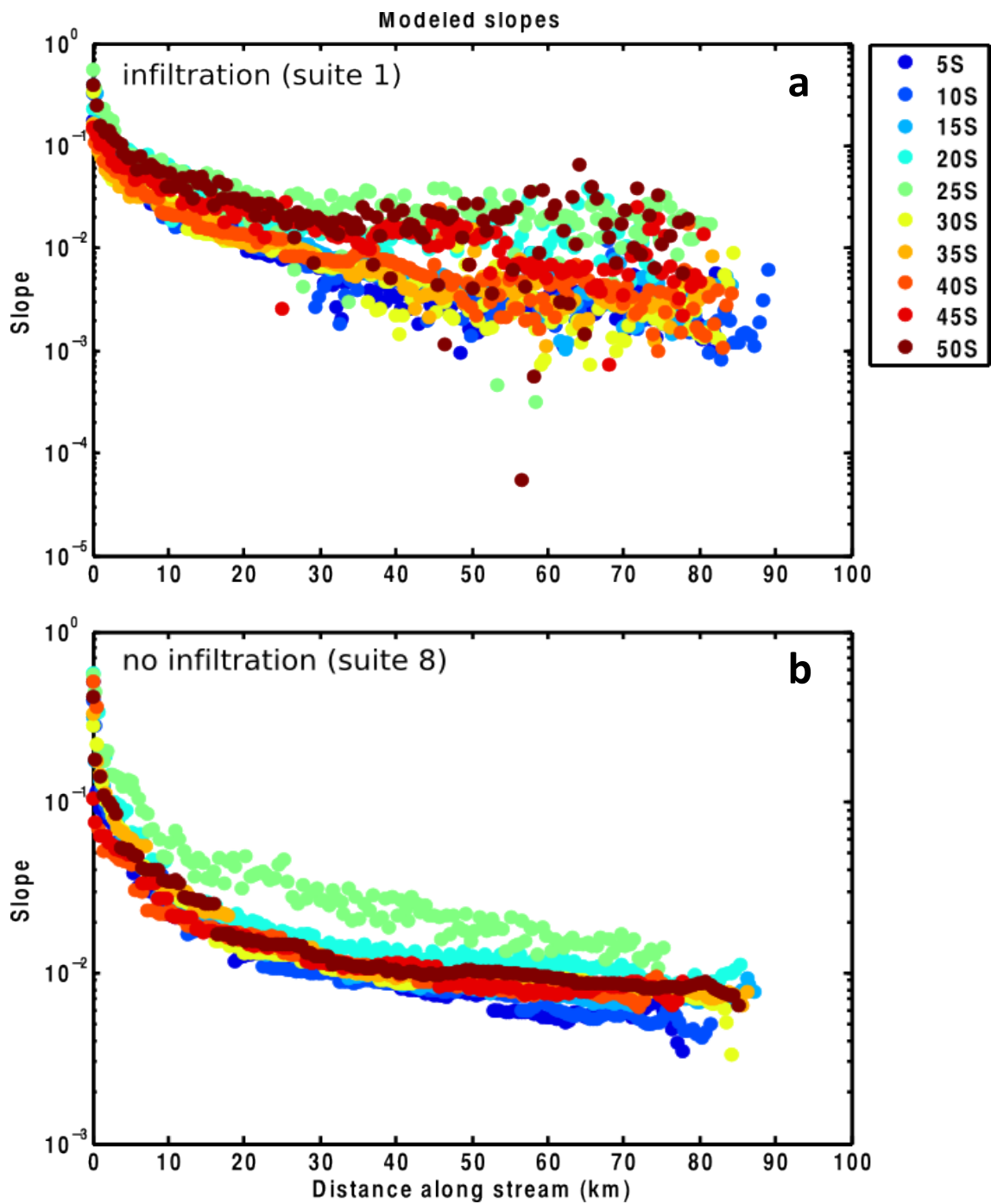


Figure 14: Modeled slopes extracted from major river channels within all 10 steady state landscapes for suite 1 (a) and suite 8 (b).

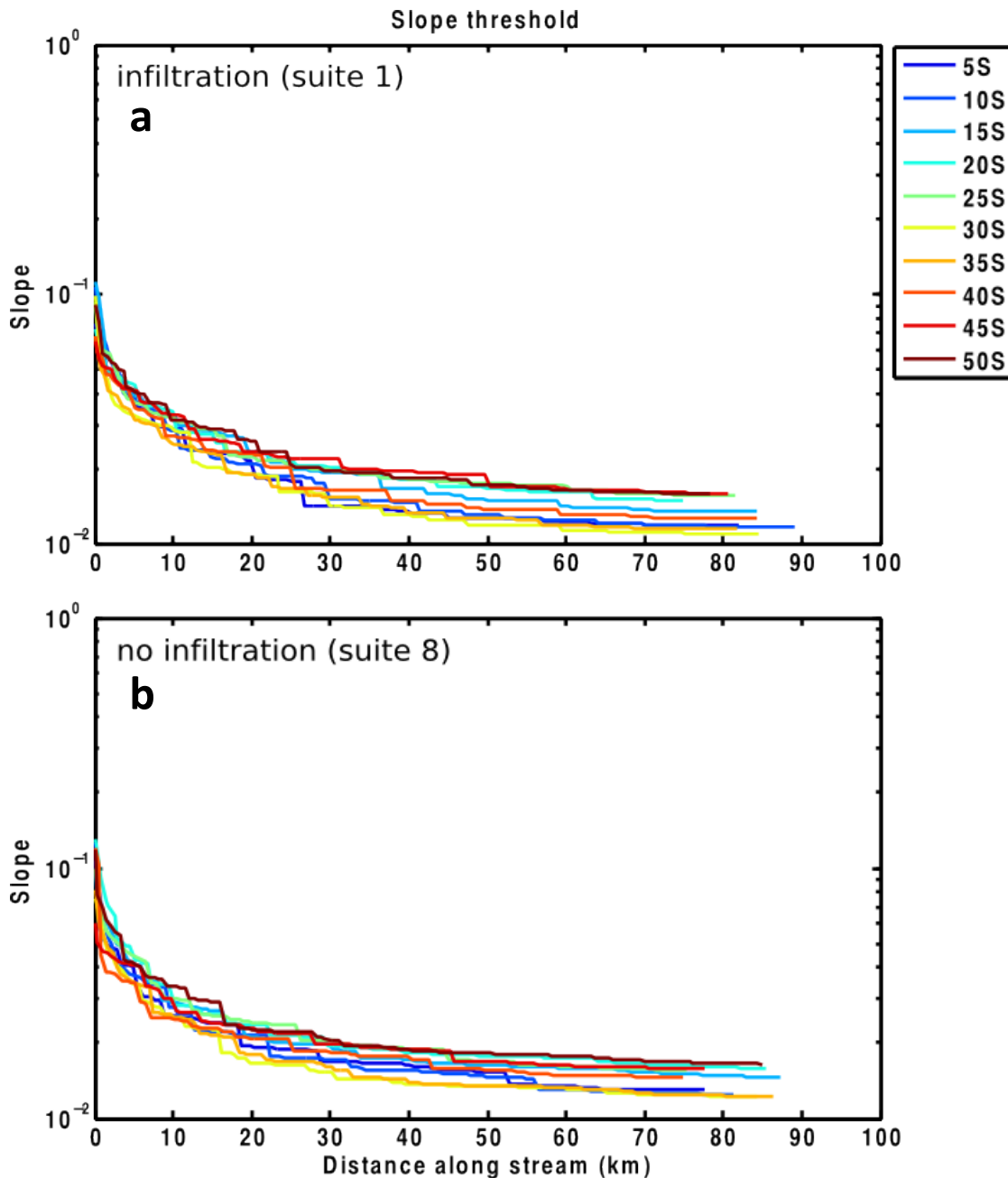


Figure 15: Theoretical threshold values for slope calculated using equation 15 along major river channels within steady state landscapes for suites 1 and 8. Values represent the slope required to generate 50 Pa and erode the bed. We use a critical shear stress of 50 Pa and mean discharge values from steady state landscapes for suite 1 (a) and suite 8 (b). Mean discharge values are calculated using equations 12 and 13.

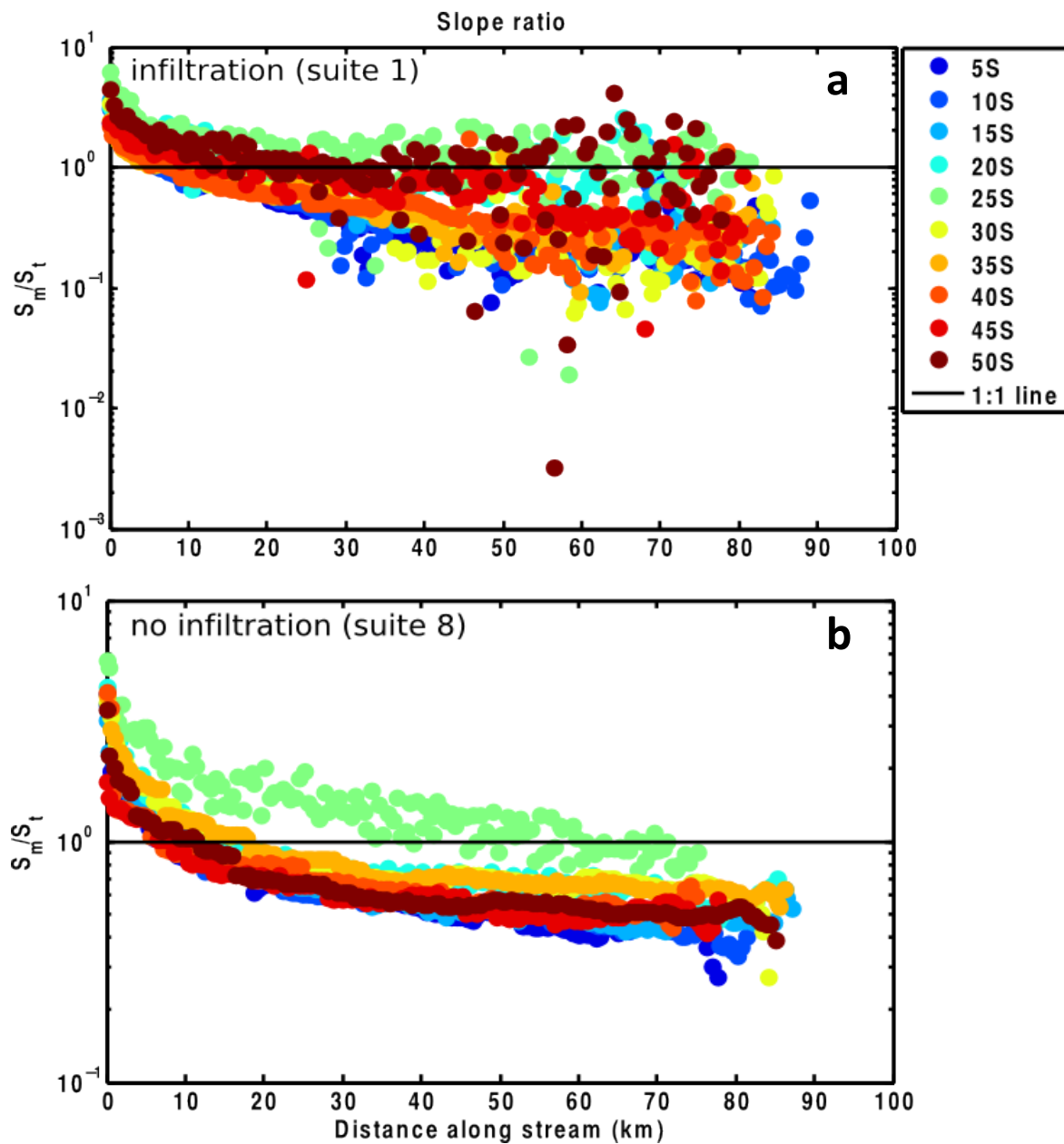


Figure 16: Ratio of modeled slopes (S_m) and theoretical threshold slopes (S_t) calculated along the length of river channels from steady state landscapes for all 10 runs in suite 1 (a) and suite 8 (b). We use mean discharge to calculate threshold slopes and it does not change from suite 1 to suite 8. Values below the 1:1 line represent points along the channel that have a larger threshold versus modeled slope and therefore mean discharge will not erode the bed. Values above the 1:1 line represent points along the channel where erosion will occur if the infiltration rate is exceeded.

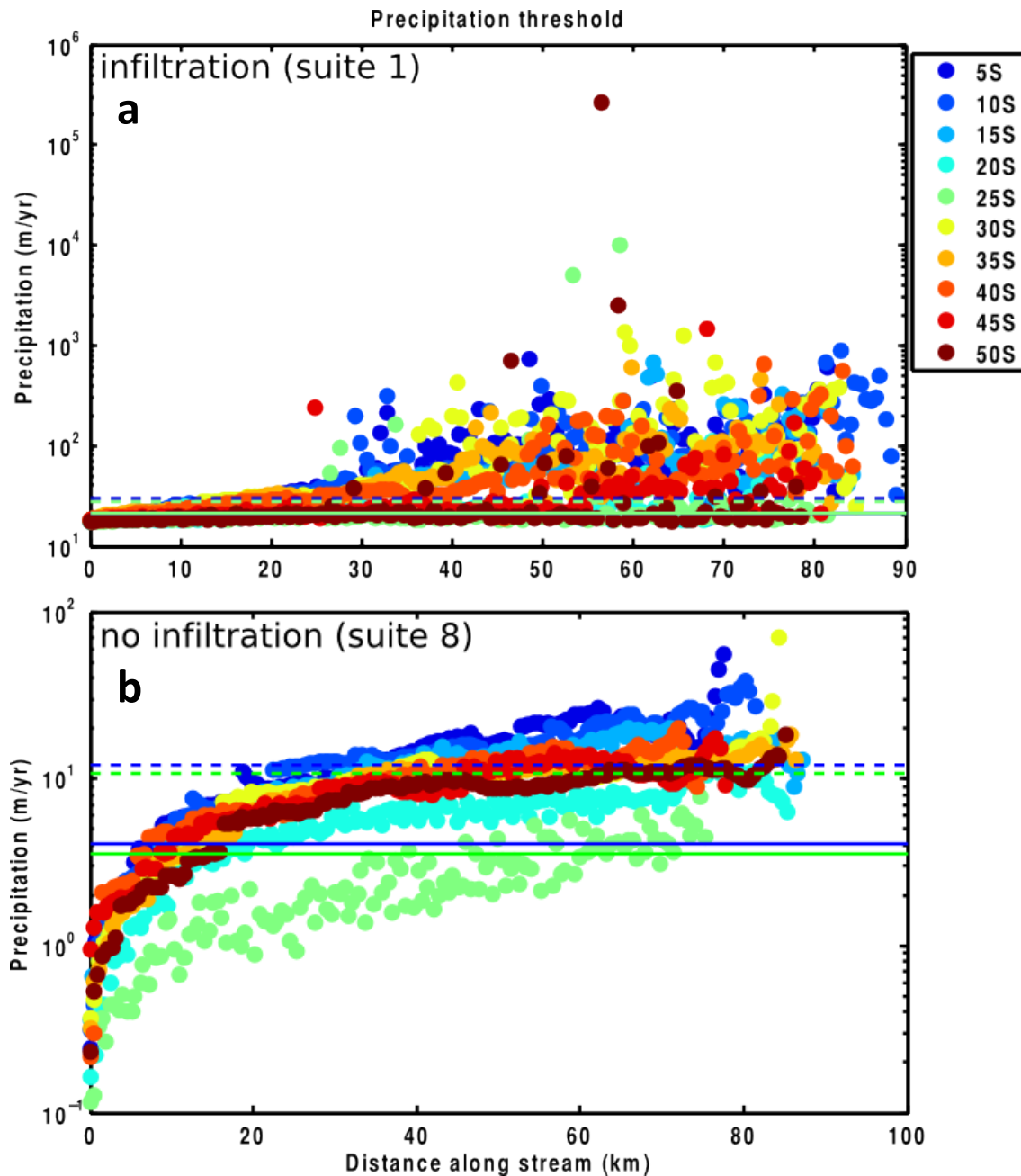


Figure 17: Theoretical threshold values for precipitation calculated using equation 16 along major river channels within steady state landscapes for suites 1 and 8. Values represent the precipitation required to generate enough discharge to erode the bed. Values are plotted along the length of each channel for all 10 landscapes from suite 1 (a) and all 10 landscapes for suite 8 (b). Solid lines represent the mean precipitation rates for 5°S (blue) and 25°S (green). Dashed lines represent the 95th percentile precipitation rates for 5°S (blue) and 25°S (green).

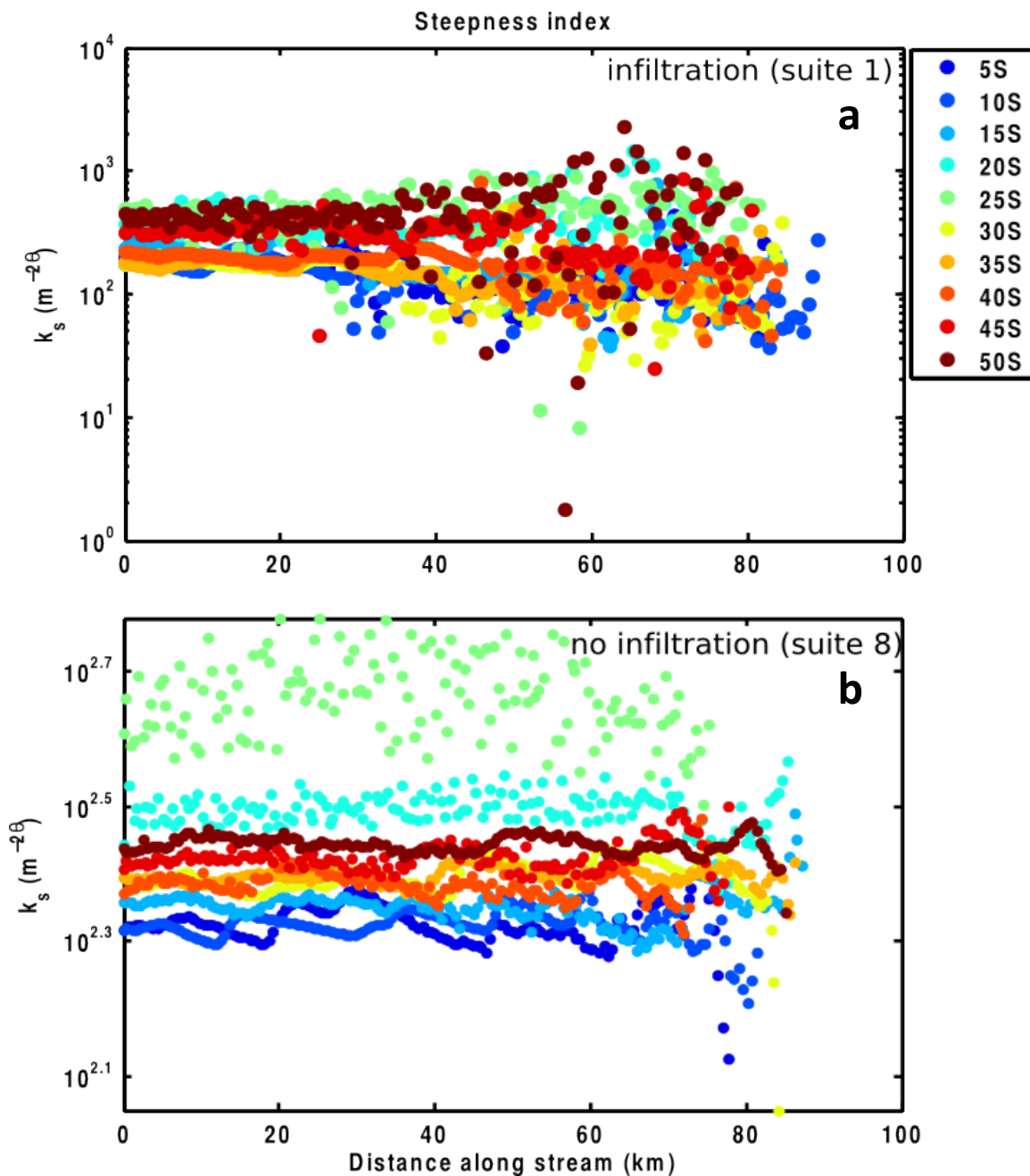


Figure 18: Steepness indices calculated using equation 17 and plotted along the length of the channel for all 10 runs from suite 1 (a) and all 10 runs from suite 8 (b). We use a concavity of 0.5. Variation is apparent in suite 1 (top) likely due to artifacts from the increased storm/inter-storm durations.

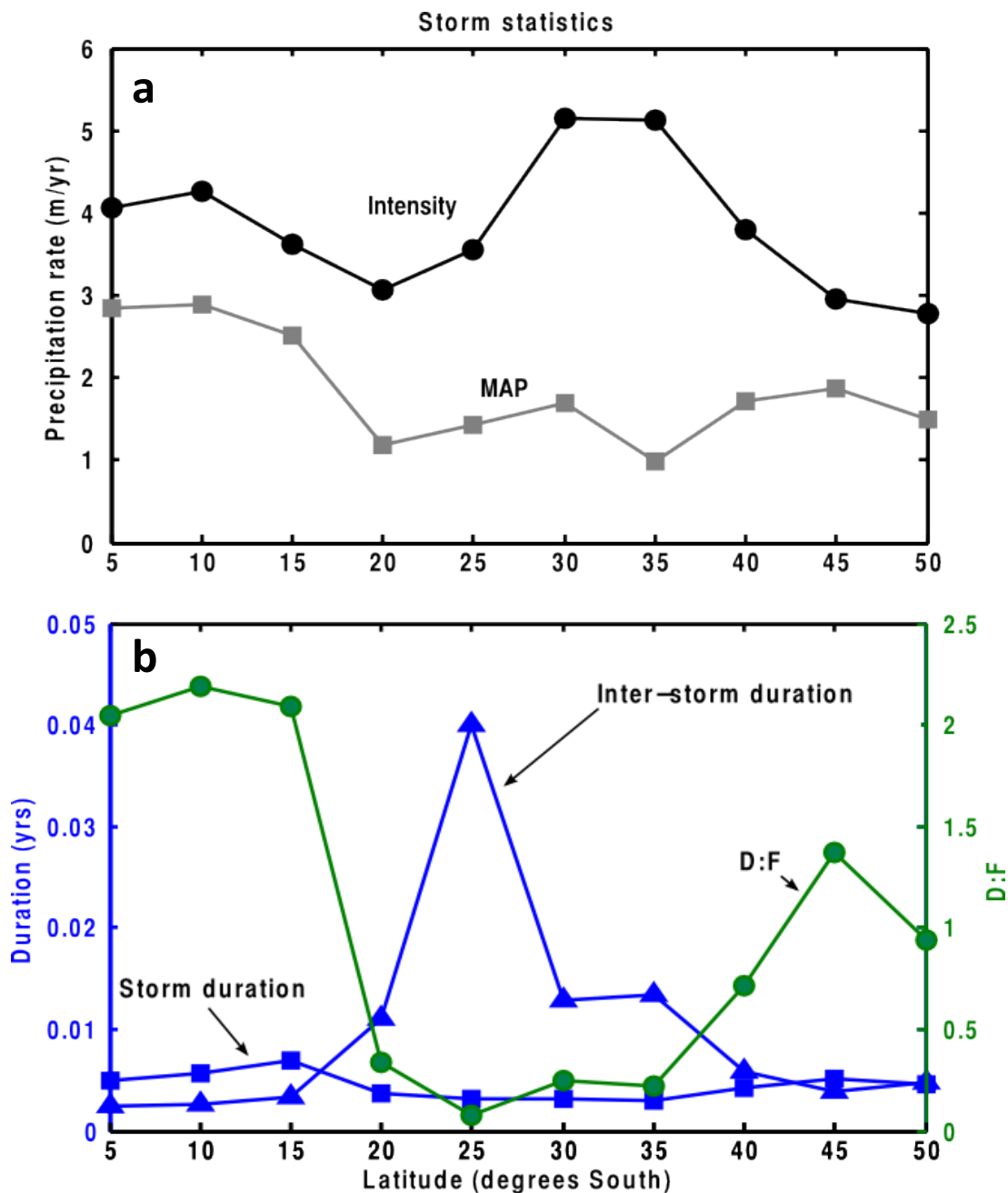


Figure 19: Mean storm statistic input values for climate parameters in CHILD model for suites 1-8. Top (a) shows the distribution of mean storm intensity (black with circles) and mean annual precipitation (MAP; gray with squares) as a function of latitude. Bottom (b) shows mean storm duration (blue with squares), mean inter-storm duration (blue with triangles) and the ratio of the two values (green with circles; D:F).

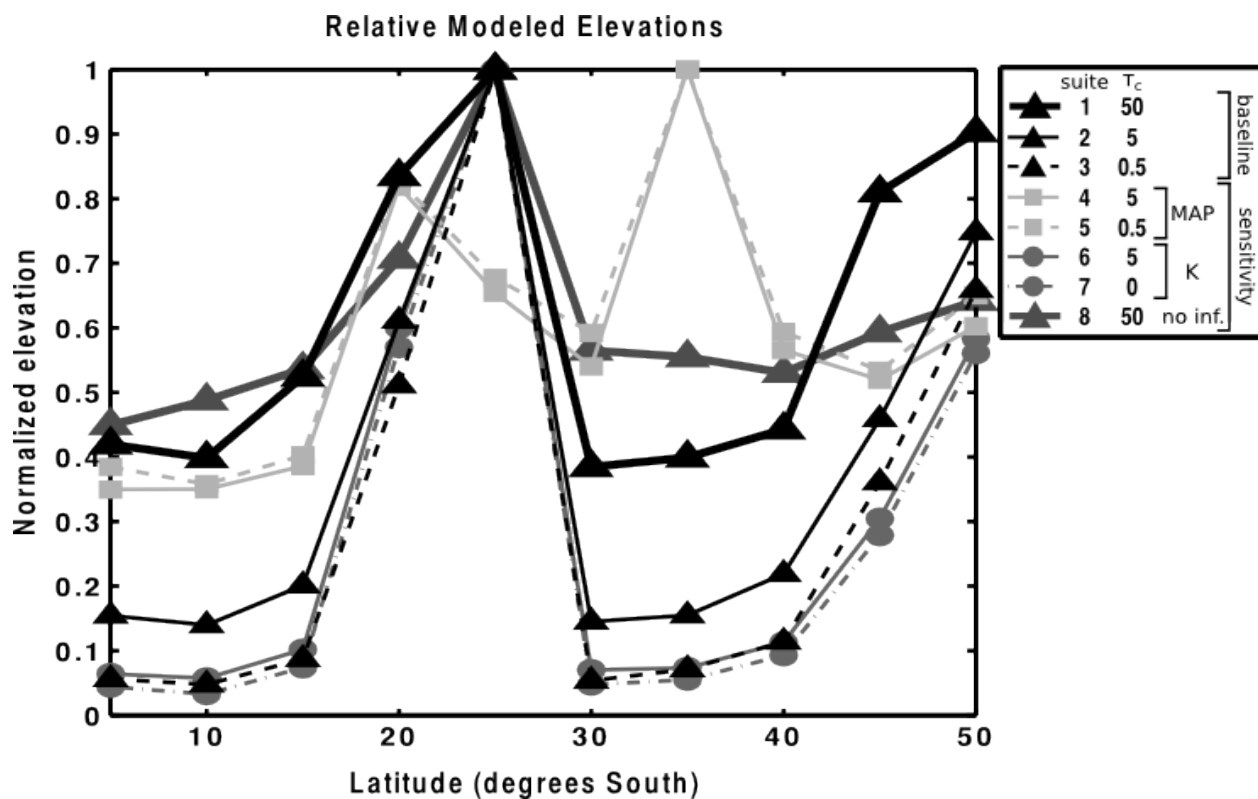


Figure 20: Maximum relative elevations from suites 1-8 plotted against their respective latitudes. Elevations are normalized using the suite of interest's maximum elevation.

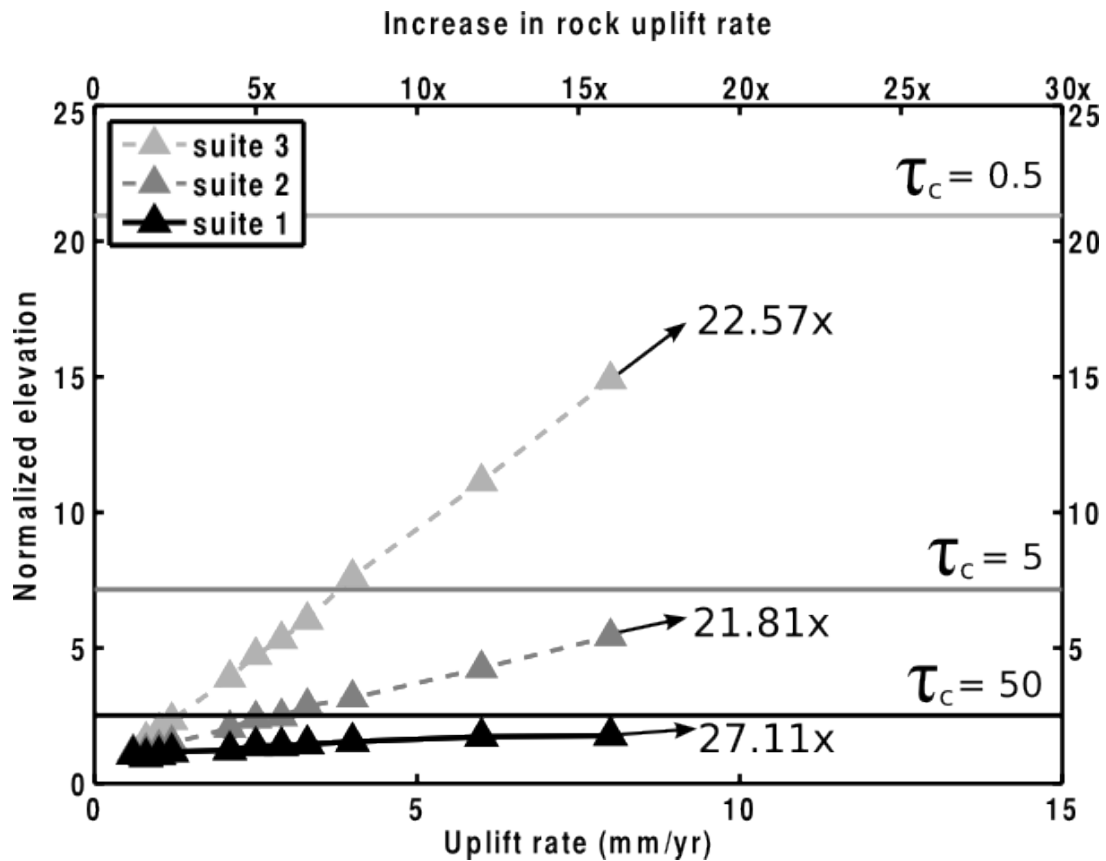


Figure 21: Projected uplift rates necessary to erase the differences in elevation generated by our climatic-dominated runs. We use climatic inputs from 10°S and increase the uplift rate with each run for suites 1-3. We fit a linear regression to project beyond our modeled analysis (arrows show the projected increase). Projected increases are shown with arrows: 22.57x (suite 3), 21.81x (suite 2) and 27.11x (suite 1). Horizontal lines represent the maximum elevations for suites 1-3. The y-axis is normalized the maximum elevation at 10°S: 1.98 km (suite1), 155.12 m (suite 2) and 61 m (suite 3) and therefore represents the increase in elevation from each increase in uplift rate.